ERDC/CRREL TR-19-20

US Army Corps of Engineers®
Engineer Research and Development Center

ERDC ENGINEER RESEARCH & DEVELOPMENT CENTER

Unmanned Aircraft Systems Sensor Integration and Innovative Construction Materials for the Arctic Program

Unmanned Aerial Systems Electromagnetic Induction Sensor Development

Evaluation of Commercial-off-the-Shelf Unmanned Aerial System Motor Interference and Mitigation in Airborne Electromagnetic Induction Sensors

Benjamin Barrowes, Dan R. Glaser, Brian G. Quinn, Mikheil Prishvin, and Fridon Shubitidze

September 2019

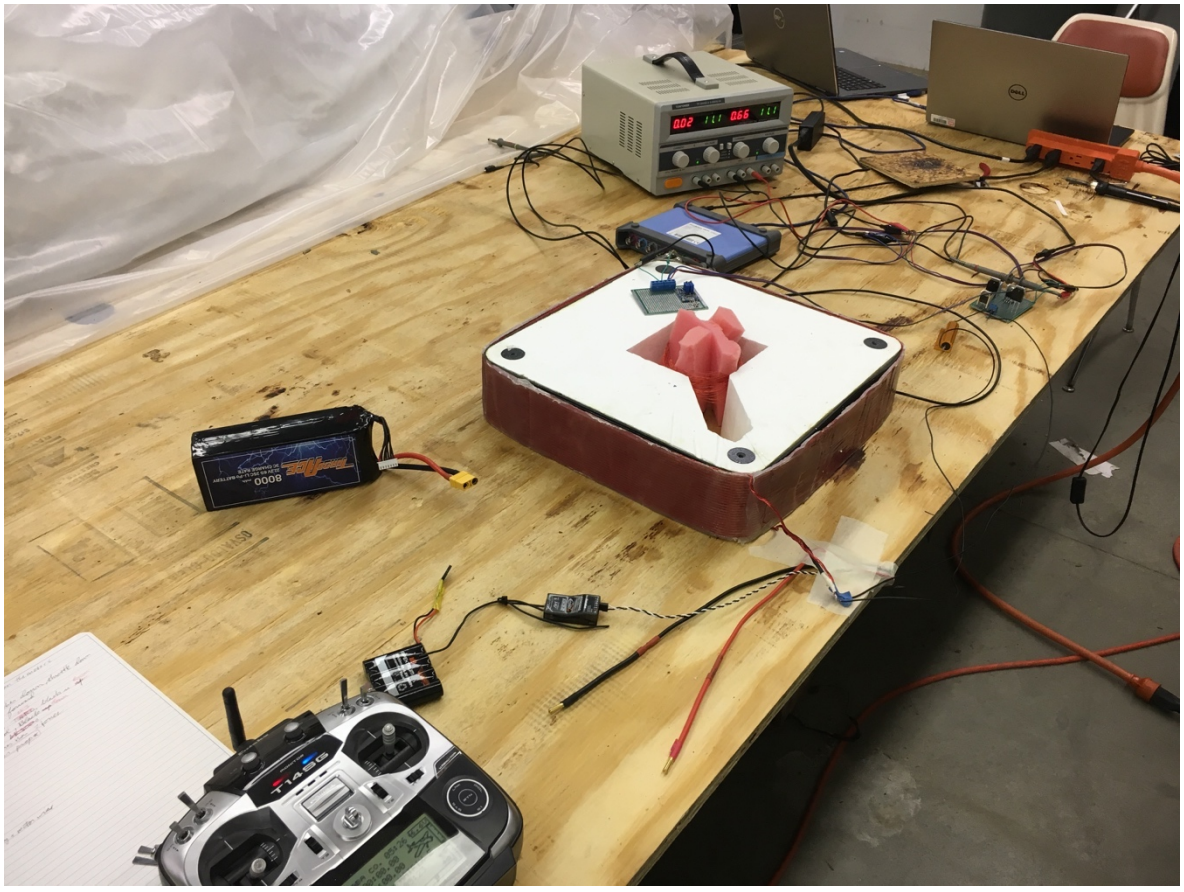

Cold Regions Research and Engineering Laboratory

The U.S. Army Engineer Research and Development Center (ERDC) solves the nation's toughest engineering and environmental challenges. ERDC develops innovative solutions in civil and military engineering, geospatial sciences, water resources, and environmental sciences for the Army, the Department of Defense, civilian agencies, and our nation's public good. Find out more at www.erdc.usace.army.mil.

To search for other technical reports published by ERDC, visit the ERDC online library at http://acwc.sdp.sirsi.net/client/default.

ERDC/CRREL TR-19-20
September 2019

Unmanned Aerial Systems Electromagnetic Induction Sensor Development

Evaluation of Commercial-off-the-Shelf Unmanned Aerial System Motor Interference and Mitigation in Airborne Electromagnetic Induction Sensors

Benjamin Barrowes, Dan R. Glaser, and Brian G. Quinn

U.S. Army Engineer Research and Development Center (ERDC)
Cold Regions Research and Engineering Laboratory (CRREL)
72 Lyme Road
Hanover, NH 03755-1290

Mikheil Prishvin and Fridon Shubitidze

Dartmouth College
Thayer School of Engineering
14 Engineering Drive
Hanover, NH 03755

Final Report

Prepared for United States Air Force Civil Engineer Center and U.S. Army Corps of Engineers
Tyndall Air Force Base, FL 32403

Under FY17 Do3F Congressional Add for “Unmanned Aircraft Systems Sensor Integration” and PE 62784/T53, “Innovative Construction Materials for the Arctic Program”

Abstract

The U.S. Army Cold Regions Research and Engineering Laboratory (CRREL) is supporting the U.S. Air Force Civil Engineer Center through research and development of an unmanned aerial system (UAS)–mounted electromagnetic induction (EMI) device capable of localizing embedded unexploded ordinance (UXO) for expedited runway and military range remediation. While EMI sensors exist for UXO detection, there are currently no UAS-based EMI systems that can provide this remote characterization of UXO with a near-real-time target classification. Developing and delivering this capability will provide a distinct improvement in soldiers' ability to quickly and efficiently recover from an attack.

Additionally, no expeditionary solutions presently exist for mapping of permafrost extent from medium-scale airborne platforms. This capability will allow lateral mapping of permafrost for impact assessments of construction activities, in a cost effective, standoff platform.

This study used the CRREL-Dartmouth-developed EMI sensor to measure the fields emitted by two different UAS motor configurations at varying standoff distances ranging from 0 to 53 cm. The minimal platform-to-sensor standoff distance was determined to be 60 cm for the planned frequency ranges. This specification will be used to design and construct the frame that carries the EMI transmitting and receiving sensor on the bottom of the UAS system.

Contents

Figures and Tables

Figures

Tables

Preface

This study was conducted to support the development of reconnaissance unmanned aerial vehicles platforms for the detection of unexploded ordinance by using time-domain electromagnetic induction technology. The Sensor Selection and Evaluation work effort is funded under the FY17 D03F Congressional Add for "Unmanned Aircraft System Sensor Integration." Additional funding was provided through the U.S. Army Corps of Engineers under PE 62784/T53, "Innovative Construction Materials for the Arctic Program." The technical monitor was Mr. Josh Fairley (CEERD-GMM).

The work was performed by the Signature Physics Branch (CEERD-RRD) and the Engineering Resources Branch (CEERD-RRE) of the Research and Engineering Division (CEERD-RR), U.S. Army Engineer Research and Development Center, Cold Regions Research and Engineering Laboratory (ERDC-CRREL). At the time of publication, Dr. M. Andrew Niccolai was Chief, CEERD-RRD; Dr. Caitlin Callaghan was Acting Chief, CEERD-RRE; and Mr. Jared Oren was Acting Chief, CEERD-RR. The Deputy Director of ERDC-CRREL was Mr. David B. Ringelberg, and the Director was Dr. Joseph L. Corriveau.

COL Teresa A. Schlosser was the Commander of ERDC, and Dr. David W. Pittman was the Director.

Acronyms and Abbreviations

ABS V	Absolute Voltage
CRREL	Cold Regions Research and Engineering Laboratory
DoD	Department of Defense
EMF	Electromagnetic Field
EMI	Electromagnetic Induction
ERDC	U.S. Army Engineer Research and Development Center
ESC	Electronic Speed Controller
ESTCP	Environmental Security Technology Certification Program
FDEMI	Frequency Domain Electromagnetic Induction
GSL	Geotechnical and Structures Laboratory
HFEMI	High-Frequency Electromagnetic Induction
IED	Improvised Explosive Devices
Rx	Receiver
SERDP	Strategic Environmental Research and Development Program
TDEMI	Time-Domain Electromagnetic Induction
Tx	Transmitter
UAS	Unmanned Aerial System
UXO	Unexploded Ordinance

1 Introduction

1.1 Background

The U. S. Army Engineer Research and Development Center (ERDC) is the lead Army research and development organization for Force Protection, Military Engineering, and Geospatial Research Engineering. The ERDC is expanding its efforts in support of new Department of Defense (DoD) protection requirements and capability gaps for troops in high-threat environments. The present work is critical to meet protection requirements and capability gaps for current research and development programs and for the planning and scheduling for future science and technology efforts within the U.S. DoD.

The Cold Regions Research and Engineering Laboratory (ERDC-CRREL) and the Geotechnical Structures Laboratory (ERDC-GSL) are supporting the U.S. Air Force Civil Engineer Center through research and development of an unmanned aerial vehicle–mounted electromagnetic induction (EMI) device capable of localizing embedded unexploded ordinance (UXO) for expedited runway and military range remediation. There are presently no standoff (no ground contact) UXO detection capabilities available to our soldiers. Developing and delivering such a capability will provide a distinct improvement in their ability to quickly and efficiently recover from an attack.

EMI is a noninvasive, standoff geophysical technique that can be used to localize and determine orientation of UXO and underground cavities caused by fragmented munitions detonation. EMI devices have long been used for mapping UXO and detecting improvised explosive devices (IED). Additionally, they have been flown on helicopter-based airborne systems for large-scale mineral exploration and groundwater applications (Barrowes and Douglas 2016). Yet, until recently, they have not been evaluated for use on unmanned aerial systems (UASs) in a reconnaissance approach. While other geophysical techniques are gaining popularity for UAS sensor implementation (Prouty and Johnson 2010; Bell 2017a, 2017b, 2018a, 2018b; Hoekstra and Mhaskar 2017; Eröss et al. 2017), EMI for UASs has not yet been successfully implemented. With that in mind, there are some academic institutions and research groups working on the problem (Auken et al. 2015; Seidel and Tezkan 2017; Kang 2018; Smith and West 1989).

Potential applications for a UAS-based EMI system are widespread from civil infrastructure, such as permafrost mapping, levee and dam assessment, slope stability assessment, and landfill characterization, to military mobility operations, including UXO and IED detection, runway remediation, and ground surface structural competency evaluations.

The initial development phases of this UAS-based EMI system require an understanding of the electromagnetic fields emitted by the UAS platform itself to optimize the performance of the system. Here we measure the fields emitted by two different UAS motor configurations at varying standoff distances from 0 to 53 cm. For this initial phase of the investigation, shielding variables are not introduced. The results from the investigation determine the minimum distance needed for the sensor to operate without negative influence from the electrical noise of the UAS motor.

The U.S. military has a need to remotely characterize in situ UXO associated with runway bombardment. While EMI sensors exist for UXO detection, there are currently no UAS-based EMI systems that can provide this remote characterization of UXO with a near-real-time target classification. The EMI sensors currently available for detection and classification of metallic UXO and IEDs are bulky and cumbersome, making it difficult to implement on a remotely controlled UAS acquisition system. ERDC-CRREL and ERDC-GSL, in conjunction with Dartmouth College, has developed or aided in the development of multiple EMI devices for detection of UXO and IEDs, including GEM-3D, MPV, MPV-II, Pedemis, and High-Frequency EMI (HFEMI) for nonmetallic UXO (Barrowes et al. 2013, 2015, 2016, 2017, 2018; Fernández et al. 2011; Sigman et al. 2017a, 2017b; Simms et al. 2017; McKenna et al. 2013; O'Neill 2016; SERDP and ESTCP 2016; Glaser et al. 2017; Glaser and Wagner 2019; Shubitidze et al. 2014a, 2014b, 2016a, 2016b; Grant et al. 2014).

1.2 Objectives

To integrate EMI sensors onto a UAS platform, either in the time domain or the frequency domain, the UAS platform itself has to be characterized electromagnetically so that the noise contribution of the UAS platform can be predicted and accounted for. Here we evaluate the noise sources associated with operating a single UAS motor under various loads and configurations. The objective is to identify a sufficient standoff distance between the motor and the EMI sensors such that the signal-to-noise ratio (SNR) is suitable for detection and characterization of UXO and IEDs. Future work

will consider the potential for additional interference from multiple motors (quad-, hex-, or octocopters).

1.3 Approach

Part of the interference expected from the UAS is from the high power-to-weight ratio electric motors on the UAS. The UAS motors typically have a pulse-width-modulated motor controller on the central part of the UAS separate from the motor body. The motor controller accepts a controlling signal from the flight controller and translates that control signal into high-current pulses that actuate the motors at different speeds.

Newer motors, such as those tested in section 3, have the motor controller integrated into the motor housing. This type of integrated motor and motor-controller combination may be advantageous to mounting an EMI instrument onto a UAS because the high-current pulses of electricity on wires from the center of the UAS to the motors at the edges of the arms of the UAS will not be necessary. This should increase the SNR in the airborne EMI data because long wires with high-current pulses on them increase noise in EMI receivers. This report looks at both motor types under different conditions and assesses the noise output from the motors, both in the frequency domain and the time domain.

The noise from both types of motors will most likely be periodic in nature, depending on the speed of the motor and revolutions per minute. During ascent and other times of increased motor activity, higher frequencies will be produced by the pulse-width-modulated motor controller. Therefore, the noise in the EMI data will not be confined to a single frequency. This complicates accounting for the noise in the data.

The most straightforward approach to minimizing the noise due to either type of motor is to separate the motor and the EMI receivers. We do this by adjusting the distance between the motors and the EMI coils, as discussed in section 3. Also, in section 3 we vary the motor output and determine the effect on noise from other factors, including the observed loading effects of the presence and absence of propellers on the motors.

We expect that mounting EMI sensors onto small, versatile, agile, and convenient UAS platforms will greatly enhance the capability and convenience of operating airborne sensors. While EMI sensors have long been used on the ground both as man-portable and cart-based modalities, automating

the process and using a standoff UAS platform could greatly reduce costs and increase safety at UXO-contaminated areas. As well, many other ground-based applications of EMI could be made quicker and more convenient by adapting them to a UAS platform. For example, using EMI for inferring the ground conductivity and permittivity would facilitate urban planning by departments of transportation. Using ground conductivity to map permafrost from a medium-scale airborne platform would represent a favorable compromise between ground-based methods, such as man-portable instruments like the EM-31, and a large, expensive helicopter-based platform, such as the Fugro RESOLVE system (Barrowes and Douglas 2016).

2 Theory

EMI is a technique that can rapidly and effectively estimate the electrical conductivity of subsurface materials to a depth of 150 m without physically contacting the surface (O'Neill 2016; Pastick et. Al. 2013). The depth of investigation and vertical resolution over the investigation depth is dependent on system design specifications; but generally, the deeper the target, the larger the target must be for detection. The electrical conductivity measurements made by EMI can be used to find metallic targets in the subsurface and to determine the frozen or unfrozen state of earth material due to the contrast in conductivity measurements between frozen and unfrozen media. Various modalities for acquiring EMI measurements exist, depending on the scope and timescale required for a given survey. These include airborne, vehicle, cart, snowmobile, boat, or handheld platforms. Airborne EMI techniques have the potential to measure terrain conditions at the tens of kilometers scale in a single day and during all seasons (Minsley et. Al. 2012; Hoekstra et al. 1975).

According to Lenz's law, a conducting object in a primary alternating magnetic field will develop eddy currents to oppose the changing flux inside the object (Wait 1951) (Figure 1). These eddy currents depend on the conductivity of the object. In metals, conductivity and electron mobility is high (often 10^7 S/m). This high conductivity allows induced opposing currents to form (again via Lenz's law) at lower frequencies than the frequencies at which induced currents form in lower-conducting materials. In other words, the time rate of change of the inducing primary field needs to be higher (higher frequency) for materials with lower conductivity. In turn, these eddy currents produce a secondary alternating magnetic field, and both the eddy currents and the secondary magnetic field they produce are out of phase with the primary field.

For frequency domain EMI (FDEMI), the component of the eddy current synchronized with the primary field is called the *in-phase component,* and 90° out-of-phase with the primary field is called the *quadrature component*. In time-domain EMI (TDEMI), the frequency-specific signatures can be seen at corresponding time intervals after cession of the transmitted current. Characteristics of these components of the secondary field are used as signatures of the target and to determine properties of the target, such as size, shape, location, orientation, permeability, and conductivity.

In general, higher conductivities and larger targets result in lower peaks in the quadrature response.

Figure 1 provides a representation of the interrelationship of the transmitted field acting on a subsurface target and the measurement of the induced secondary field at the receiver coil. The transmit coil propagates an alternating magnetic field, which induces volume and surface eddy currents in the target. The induced currents produce a secondary alternating electromagnetic field. The equations governing electromagnetic induction for the surroundings of the target are

$$\nabla^2 \Psi = 0, \tag{1}$$

where Ψ is the scaler potential of the magnetic field (T • m^2).

The magnetic field within the target is governed by

$$\nabla^2 \overline{\Pi}_2 + k^2 \overline{\Pi}_2 = 0, \tag{2}$$

where $\overline{\Pi}_2$ is the secondary magnetic field (A • m^{-1}) and k is the wave number of the target's material (m^{-1}) (O'Neill 2016; Cheng 1989).

Figure 1. Schematic of a typical electromagnetic induction system. Current in the transmit coil creates an alternating magnetic primary field. This field induces an alternating dipole moment in the target, which leads to a secondary magnetic field. This induced secondary field is detected by the receive coil, by which the target can be located.

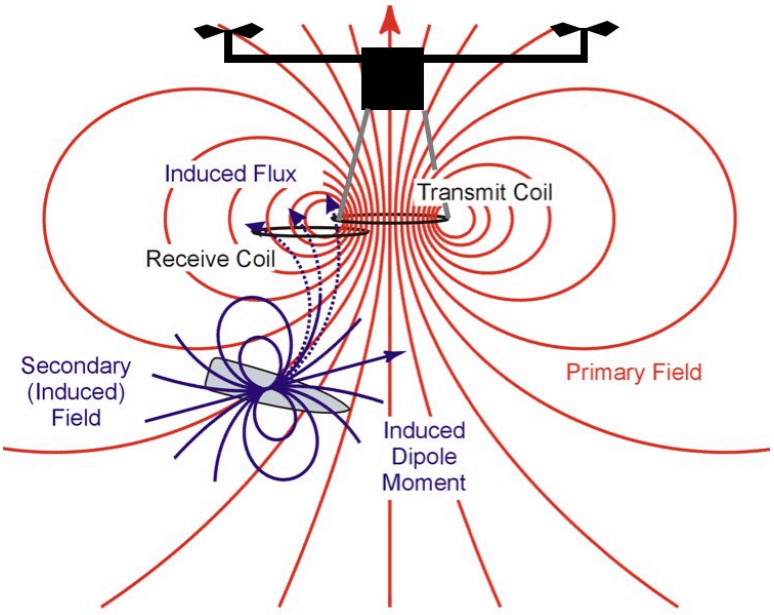

The frequency at which the quadrature component of the secondary field is maximum is determined by the size, shape, permeability, and conductivity of the target. This is the relaxation peak, which generally is reduced by increased target size and reduced by increasing conductivity (O'Neill 2016). Often, a priori knowledge of the target properties or range of target properties is used to classify target signatures.

3 Laboratory Methods

This effort measured a total of 45 individual test configurations in the Electromagnetics Laboratory at CRREL in Hanover, New Hampshire. A time-domain electromagnetic induction system was assembled to assess the impact of UAS motor electromagnetic interference on the detection of UXO. Section 3.1 describes the system components, and section 3.2 describes the two motors used in the test. Section 3.3 discusses the two test targets, and section 3.4 addresses the influence of a carbon frame. Finally, section 3.5 provides the test matrix detailing the physical changes between each measurement. Glaser et al. (2018) present a high-level summary of the findings in relation to the measurement of petrophysical properties through time-domain-induced polarization measurements.

3.1 EMI sensor configuration

The TDEMI system in development consists of a PicoScope model 4824, a Tekpower TP3005D-3 direct current power supply, a data-logging computer, a square transmitter (Tx) wire loop (34 cm × 34 cm) with 24 turns, and a receiver (Rx) wire coil (7.5 cm diameter) with 100 turns (Figure 2).

Figure 2. The research and development TDEMI system showing the bench-scale test components and the UAS components. Specifically, we show the 4824 PicoScope; the Tx power supply, a Tekpower TP3005D-3; and Tx/Rx coil configuration. The UAS components consist of the motor, motor controller, remote control, and power supplies.

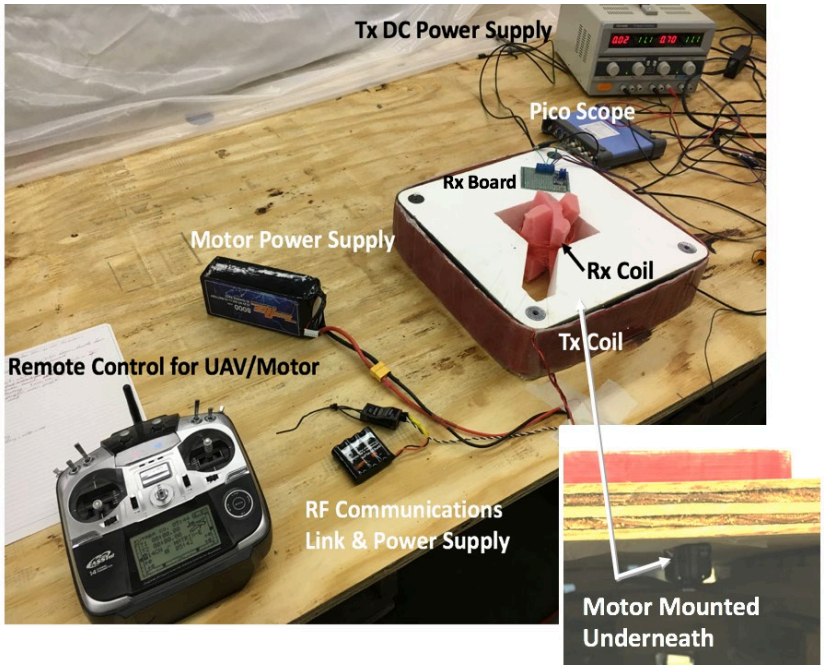

While the motor is below the sensor, the motor is inverted in the direction it would be if it was above the sensor. Since the sensor measurement is the same above and below, the signature of the motor is replicated as it would be expected in a true deployment.

3.2 UAS motors

We evaluated electromagnetic interference for two common UAS motor configurations at standoff distances of 0 cm, 32.5 cm, and 53 cm (Figure 3). An older-style propeller motor, TA-INF9-22, requiring a separate motor controller (also known as an ESC [electronic speed controller]) was investigated. The Turbo Ace TA-INF9-24 is an ESC that is located close to the body of the UAS. This introduces a large electromagnetic field (EMF) footprint due to the wiring associated with the separation of the motor and the motor controller. However, the newer-style motor, Hitec RCD USA Inc. Energy Propel 4108/40 CCW, moves the controller to the motor itself, limiting the spatial footprint of the source of EMF contamination.

Figure 3. (*A*) An older style propeller motor, TA-INF9-22, which requires a separate motor controller, the Turbo Ace TA-INF9-24. (*B*) Newer style motor with integrated motor controller.

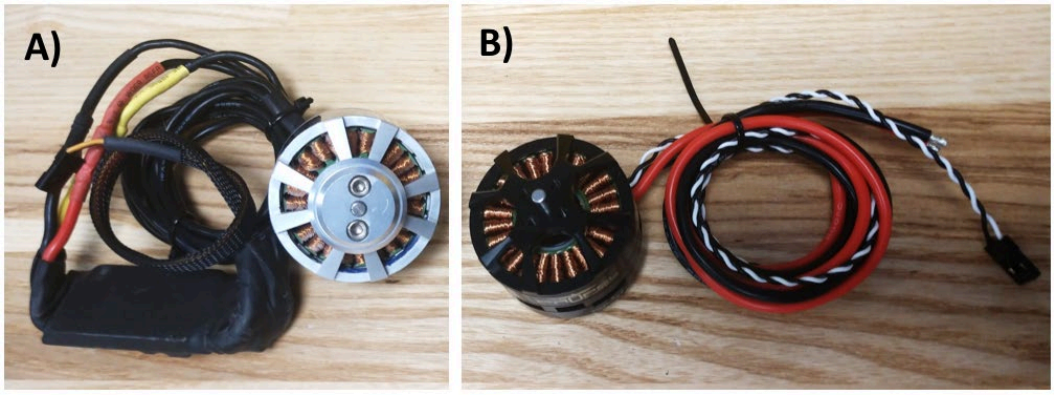

The motors are both controlled by a Futaba 14SGH 14-Channel 2.4 Hz Computer Radio System, displayed in Figure 2.

3.3 Targets and calibration

Two targets were used in the initial calibration of the system: a steel cylinder target with dimensions of 1 cm diameter by 3 cm in height and an inert 40 mm munitions shell (Figure 4). However, the majority of the testing used the inert 40 mm munitions shell.

Figure 4. Targets used in this investigation include (*A*) a 1 cm × 3 cm steel rod and (*B*) an inert 40 mm munitions shell.

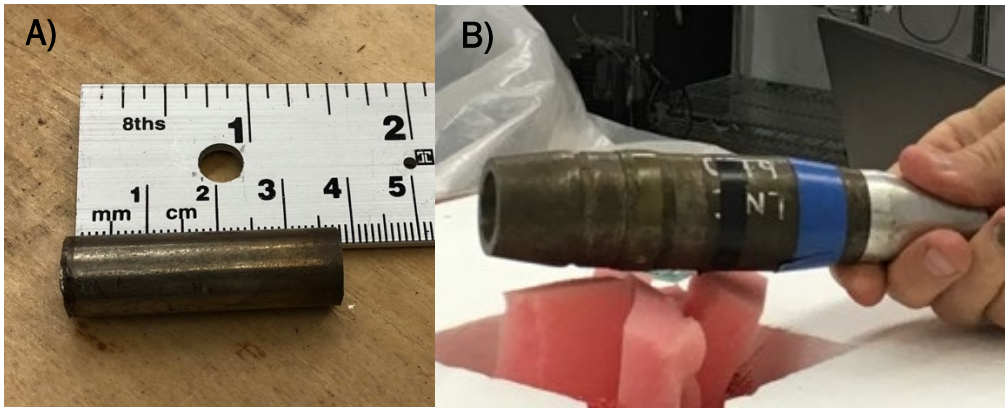

3.4 Carbon fiber frame

In addition to the motor testing, we took the opportunity to confirm that no additional signal would be present from the carbon fiber frame we are building to support the EMI antennas under the UAS (Figure 5). This was a qualitative test with no data file recorded. A selection of two types of 1.2 m lengths of angled carbon fiber stock (8 × 140 g and 2 × 65 g) were placed directly under the Tx/Rx sensor. No response from the carbon fiber stock was seen in the signal, which is expected due to the lower conductivity of carbon fiber requiring higher frequencies (or quicker turnoff times) to display an inductive response (Sigman et al. 2017b; Barrowes et al. 2016).

Figure 5. Carbon fiber bundle used in the test (8 × 140 g angled carbon fiber and 2 × 65 g).

3.5 Test-configuration matrix

Table 1 presents the overall configuration matrix for this series of tests. Sections 3.5.1 through 3.5.6 describe the configuration for each group of tests and the general intent behind each test.

Table 1. The test-configuration matrix provides a detailed list of variable conditions during each test.

	Test ID	Tx/Rx to Motor (cm)	Motor Status	Target	Tx/ Rx to Target (cm)	Motor Interference Present	Target Response Detected	Notes
Background EMF	1	0	OFF	--	--	--	--	Background, Half-Period Recorded
	2	0	OFF	--	--	--	--	Background
	3	0	OFF	--	--	--	--	Background, Lights Off
	4	0	OFF	--	--	--	--	Background
	5	0	OFF	--	--	--	--	Lights Off
	6	0	OFF	--	--	--	--	Repeat of 5 / Amplifier Repaired
	7	0	OFF	--	--	--	--	
	8	0	OFF	--	--	--	--	Data file irretrievably corrupted
Target Calibration	9	0	OFF	Steel Cylinder	0	--	--	1cm x 3c steel cylinder
	10	0	OFF	--	--	--	--	
	11	0	OFF	40mm	5	--	YES	
Static & Varying Speed Motor Response	12	0	OFF	--	--	YES	--	Hooking up motor and battery signal
	13	0	25%	--	--	YES	--	Propellers Attached
	14	0	50%	--	--	YES	--	Propellers Attached
	15	32.5	OFF	--	--	--	--	Background, Propellers Attached
	16	32.5	25%	--	--	YES	--	Propellers Attached
	17	32.5	50%	--	--	YES	--	Propellers Attached
	18	32.5	OFF	--	--	--	--	Spectrum up to 500kHz
	19	32.5	25%	--	--	YES	--	Spectrum up to 500kHz
	20	32.5	50%	--	--	YES	--	
Static & Varying Speed w/ Standoff & Target	21	32.5	OFF	--	--	--	--	No Motor Background
	22	32.5	OFF	40mm	5	--	YES	No Motor Background
	23	32.5	25%	40mm	5	YES	YES	
	24	32.5	50%	40mm	5	YES	YES	Data file irretrievably corrupted
	25	32.5	25%	40mm	5.5	YES	YES	Repeat 23
Static & Varying Speed Motor Response	26	32.5	25%	--	--	NO	--	New Motor, No Propellers
	27	32.5	50%	--	--	NO	--	New Motor, No Propellers
	28	32.5	25%	--	--	YES	--	Spectrum up to 500kHz
	29	32.5	50%	--	--	YES	--	Spectrum up to 500kHz
	30	32.5	OFF	--	--	--	--	Old Motor, No Propellers
	31	32.5	25%	--	--	YES	--	Old Motor, No Propellers
	32	32.5	50%	--	--	YES	--	Old Motor, No Propellers
	33	32.5	OFF	--	--	--	--	Old Motor, Propellers Attached
	34	32.5	25%	--	--	YES	--	Data file irretrievably corrupted
	35	32.5	50%	--	--	YES	--	Old Motor, Propellers Attached
	36	32.5	OFF	--	--	--	--	New Motor, Propellers Attached
	37	32.5	25%	--	--	YES	--	New Motor, Propellers Attached
	38	32.5	50%	--	--	YES	--	New Motor, Propellers Attached
	39	0	OFF	--	--	--	--	New Motor, Propellers Attached
	40	0	25%	--	--	YES	--	New Motor, Propellers Attached
	41	0	50%	--	--	YES	--	New Motor, Propellers Attached
	42	53	OFF	--	--	--	--	New Motor, Propellers Attached
	43	53	25%	--	--	NO	--	New Motor, Propellers Attached
	44	53	50%	--	--	YES	--	New Motor, Propellers Attached
CF	45	--	OFF	Carbon Fiber Bundle	0	--	--	See description in section 3.5

3.5.1 Background electromagnetic field characterization (Tests 1–8)

Tests 1–8 represent the initial system functionality assessment and background conditions, examining the environmental factors within the laboratory that may cause interferences. Specifically, there was some concern

that EMFs from the overhead lighting may be observed at the 60 Hz frequency in the measured data. Background conditions were shown to be relatively clean of interference sources.

3.5.2 Target calibration (Tests 9–11)

Tests 9–11 represent measured target responses for a 1 cm diameter by 3 cm long steel cylinder and an inert 40 mm munition. By measuring the responses prior to initiating the motor, we established the unimpeded signature for each target.

3.5.3 Static- and varying-speed motor response (Tests 12–20)

Tests 12–14 were conducted with no standoff and no target. Motor operational configurations included off, 25%, and 50% duty cycles. Duty cycles above 50% were not evaluated as they will not be experienced under the expected concept of operations. Tests 15–20 implemented the same approach but with a standoff of 32.5 cm. Additionally, Tests 18, 19, and 20 examined a frequency domain spectrum of 12 Hz up to 500 kHz; all of the other tests are time domain. Since the electrical noise from the running motors is an unknown quantity, for these tests we review the spectrum to ensure that our time-domain system operates at an optimum frequency and that no frequency-dependent response is negatively impacting the data.

3.5.4 Static- and varying-speed motor response with targets (Tests 21–25)

Tests 21–25 provide EMI signatures for an inert 40 mm target 5 cm from the Tx/Rx coil. These tests used a constant standoff distance between the sensor and the motor of 32.5 cm and included varying motor speeds of off, 25%, and 50% duty cycles.

3.5.5 Standoff static- and varying-speed motor response (Tests 26–44)

Tests 26–38 repeat the configuration in the previous set of tests without the inert 40 mm target, using both the TA-INF9-22 and Hitec motors. These tests evaluate the additional loading on the motor from the propellers.

Tests 39–40 repeat the same tests but change the motor to a Tx/Rx coil distance of 0 cm.

Tests 41–44 examine an increase in the distance between the motor and the Tx/Rx coil (53 cm).

3.5.6 Carbon fiber frame response (Test 45)

Test 45 investigated the response of two types of 1.2 m length carbon fiber angled stock, gathered as a single bundle, as described in section 3.4.

4 Results and Discussion

Appendix A provides a full suite of signatures for each of the 45 measurements. The following subsections present characteristic responses for the various test case groupings of background EMF characterizations, target calibration, static- and varying-speed motor response, static- and varying-speed motor response with targets, and carbon fiber frame response. Note that all results presented are unprocessed data, with the exception of calculating the absolute value in instances where negative data were recorded. Another important consideration is that much of the observed background noise can be reduced through stacking and low-pass filters.

4.1 Background electromagnetic field characterization (Tests 1–8)

Tests 1–8 represent initial system functionality assessment and background conditions, examining the environmental factors within the laboratory that may cause interferences. Specifically, there was some concern that EMFs from the overhead lighting may be observed at the 60 Hz frequency in the measured data. The results demonstrated that background conditions were relatively clean of electrical interference sources, with no observable variations in measured voltage in the 60 Hz frequency range on Tests 1–8.

4.2 Target calibration (Tests 9–11)

Tests 9–11 represent measured target responses for a 1 cm diameter by 3 cm length steel cylinder and an inert 40 mm munition test analogue. By measuring the responses prior to initiating the newer motor, we established the unimpeded target signature. Figure 6 shows target signatures relative to the signature associated with a motor at a standoff distance of 0 cm. At this distance, it is clear that the metal of the motor results in a measurable signature although it is of a smaller relative magnitude when compared to the steel cylinder and inert 40 mm targets.

Figure 6. The measured response of the motor in an off configuration and the targets at 0 cm.

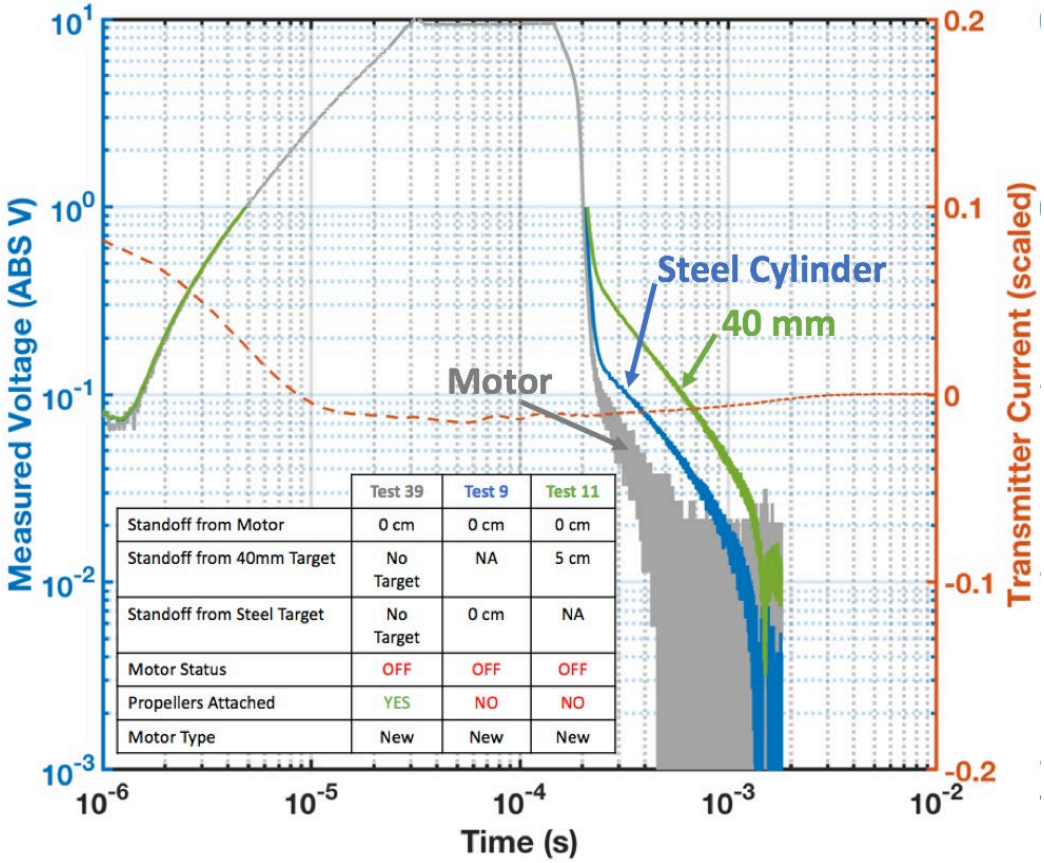

4.3 Static- and varying-speed motor response (Tests 12–20)

Tests 12–14 were conducted with no standoff and no target. Each motor was tested in the off, 25%, and 50% duty-cycle configurations. Tests 15–20 implemented the same approach but with a standoff of 32.5 cm. Additionally, Tests 18, 19, and 20 examined a spectrum output up to 500 kHz. Analyzing the spectrum allowed for identification of frequency-dependent signatures that might affect the operational frequency for the time-domain system. With the exception of Test 12 and 15 where the motor was off, Tests 13, 14, 16, and 17 presented responses, in the form of measured voltage changes, at regular intervals that correspond to the rotational frequency of the individual motors. Note when the motors are operated at a 25% duty cycle, the regular interval response from the motor is approximately half the rate of the response noted when the motors operate at a 50% duty cycle. This response appears as noise in the data, but in fact it is a predictable response that can be compensated for if necessary (Figure 9; Appendix A, Figures A-13 and A-14.

4.4 Static- and varying-speed motor response with standoff and targets (Tests 21–25)

Tests 21–25 provide EMI signatures for an inert 40 mm target 5 cm from the Tx/Rx coil. These tests used a constant standoff distance between the sensor and the new motor of 32.5 cm and included varying motor speeds of off, 25%, and 50% duty cycles. Test 21 is a background measurement without a target present. Test 22 has a target present but the motor is not engaged. Test 23 has a target at 5 cm, and the motor is engaged at a 25% duty cycle. Test 24 is the same as Test 23, but the duty cycle is increased to 50%. Test 25 is a repeat of Test 23. On review of the resulting data, it became evident that Test 24, the 50% duty-cycle data, was corrupted. Figure 7 shows the results of Tests 21, 22, and 25. This effectively conveys the ability of the TDEMI system to detect a target in an operational UAS motor environment and shows the responses observed for the inert 40 mm target with the motor operating at 25% (blue) and with the motor off (yellow), relative to the background response of the motor with no target (gray).

Figure 7. Tests 21, 22, and 25 represent the conditions of no target, target, and target with 25% motor power.

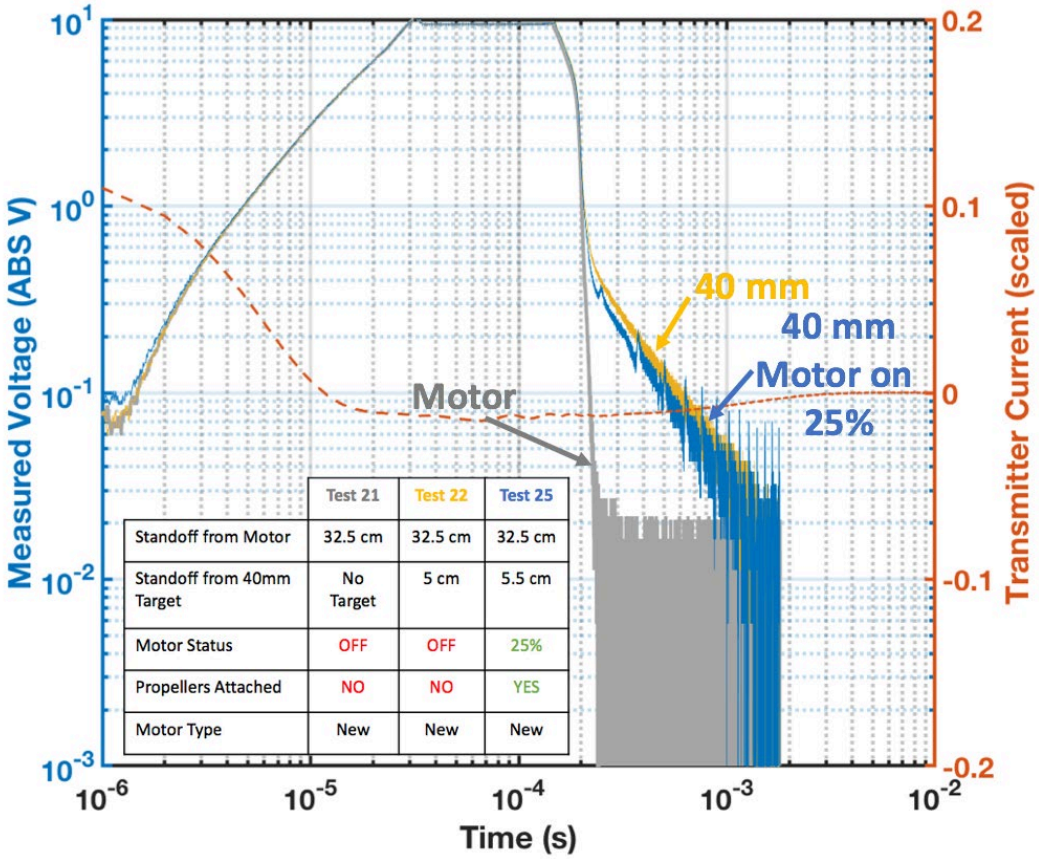

4.5 Standoff static- and varying-speed motor response (Tests 26–44)

Tests 26–27 use the new motor at varying speeds with the propellers detached and at a standoff distance of 32.5 cm. Tests 28–29 use the same configurations but record the frequency spectrum.

Tests 30–32 examine the motor with separate motor controller at varying speeds with an offset of 32.5 cm and the propellers detached. Tests 33–35 follow the same configuration but with the propellers attached. Figure 8 shows the signal associated with the motors in operation while Figure 9 demonstrates the old and new motors with and without propellers attached. Additionally, Figures 9c and 9d illustrate the regularity of the signal associated with the motor and propellers. Notably, in Figure 9, the addition of the propellers, which are of negligible weight and wind resistance, added an observable increase in noise due to the loading on the motor. This is important as it suggests that, with a full payload, the signal associated with loading on the motor could be significant, reducing the overall SNR.

Figure 8. Responses for the old and new motors operating at 50% are shown with the transmitted current. Note the measurement configuration for the old motor did not include the motor controller in the sensing region of the Tx/Rx coil. Thus, we expected an even greater interference on the older motors than what is presented.

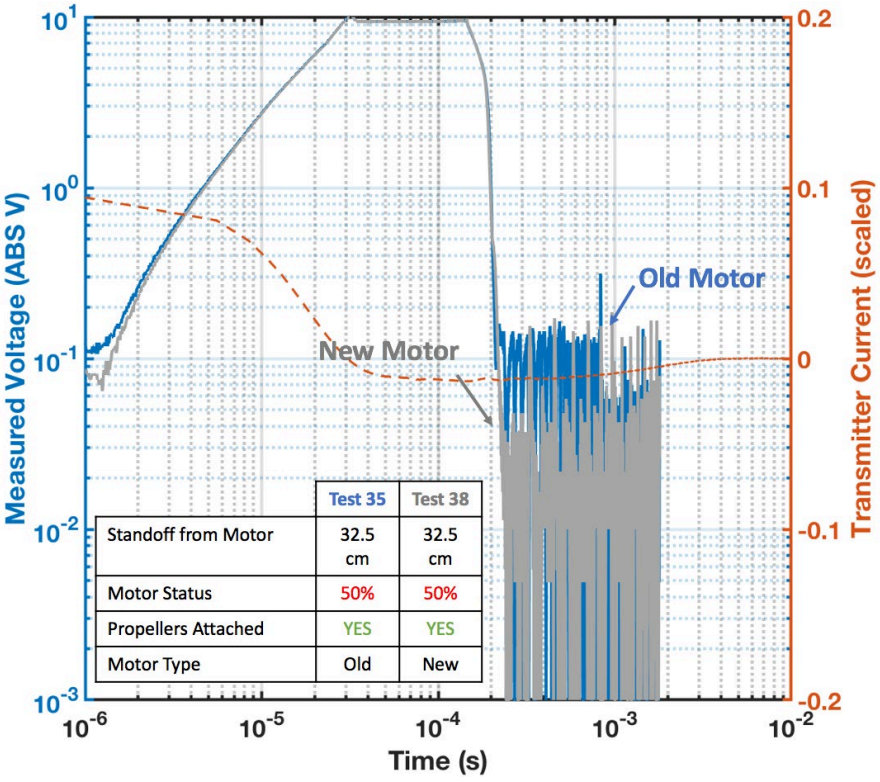

Figure 9. Responses for the old motor (*A* and *C*) and the new motor (*B* and *D*) with (*blue*) and without propellers (*gray*). This demonstrates the additional power load exhibited by the motor when the propellers are in place and shows the overall decrease in noise associated with the newer motor. (*C*) and (*D*) show the recorded data on a linear scale rather than the log-log plots displayed in (*A*) and (*B*). This better displays the regular cycle frequency of the motors. It also highlights the relative stability achieved in the newer motor. The regular cycling shown in the new motor will allow for a more effective data filter design for low signal responses.

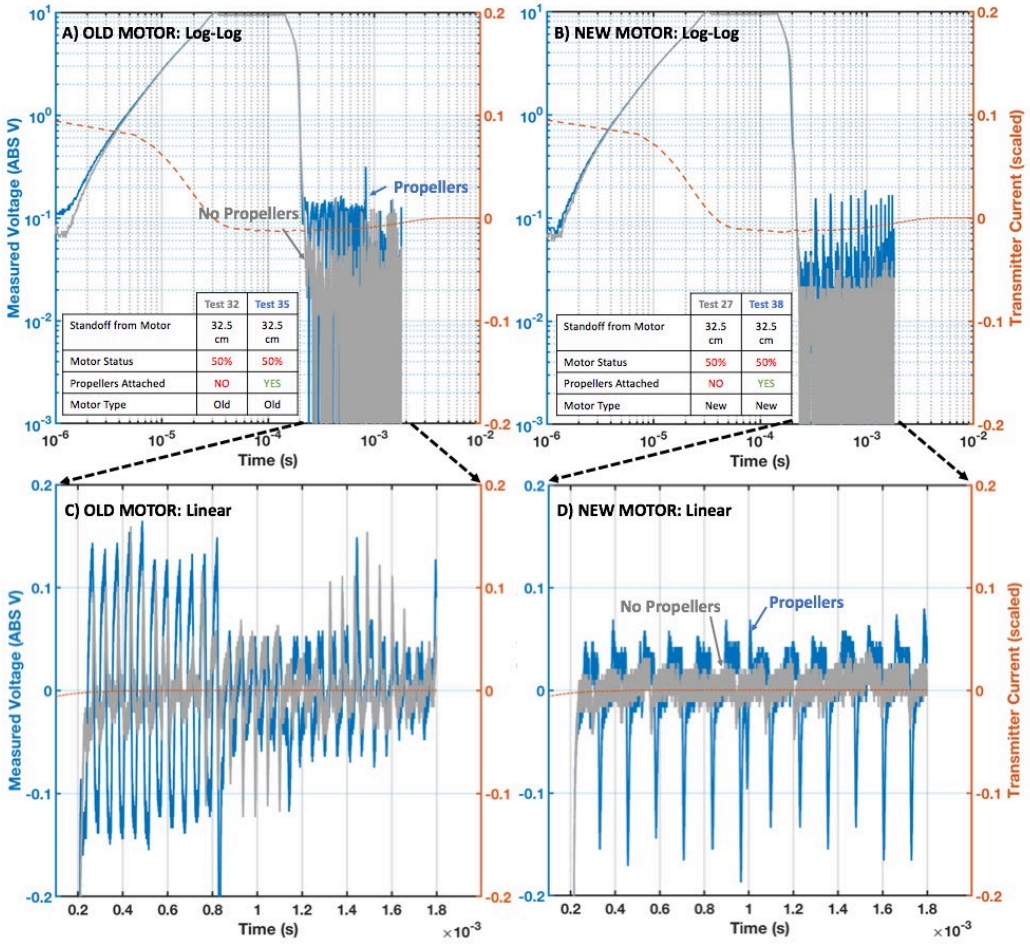

Tests 36–44 use the new motor at three standoff distances 0 cm, 32.5 cm, and 53 cm and at varying speeds. For all of these tests, the propellers are attached. Figure 10 shows the results of the UAS motor interference in three different operating conditions, off, 25%, and 50% power, for three different standoff distances: 0, 32.5 cm, and 53 cm. Test 39 shows a clear inductance response from the motor, itself being in close proximity to the Tx/Rx coil. This response is still observed in Test 40 with the motor engaged at 25% power level; additionally, significant noise is present from the electromagnetic field associated with the operating motor. In Test 41, the inductive signature of the motor is no longer distinguishable from the electromagnetic noise associated with the running motor at a 50% power level.

Figure 10. Results matrix for varying motor power and standoff distance. Notice the reduction in noise with increasing standoff distance.

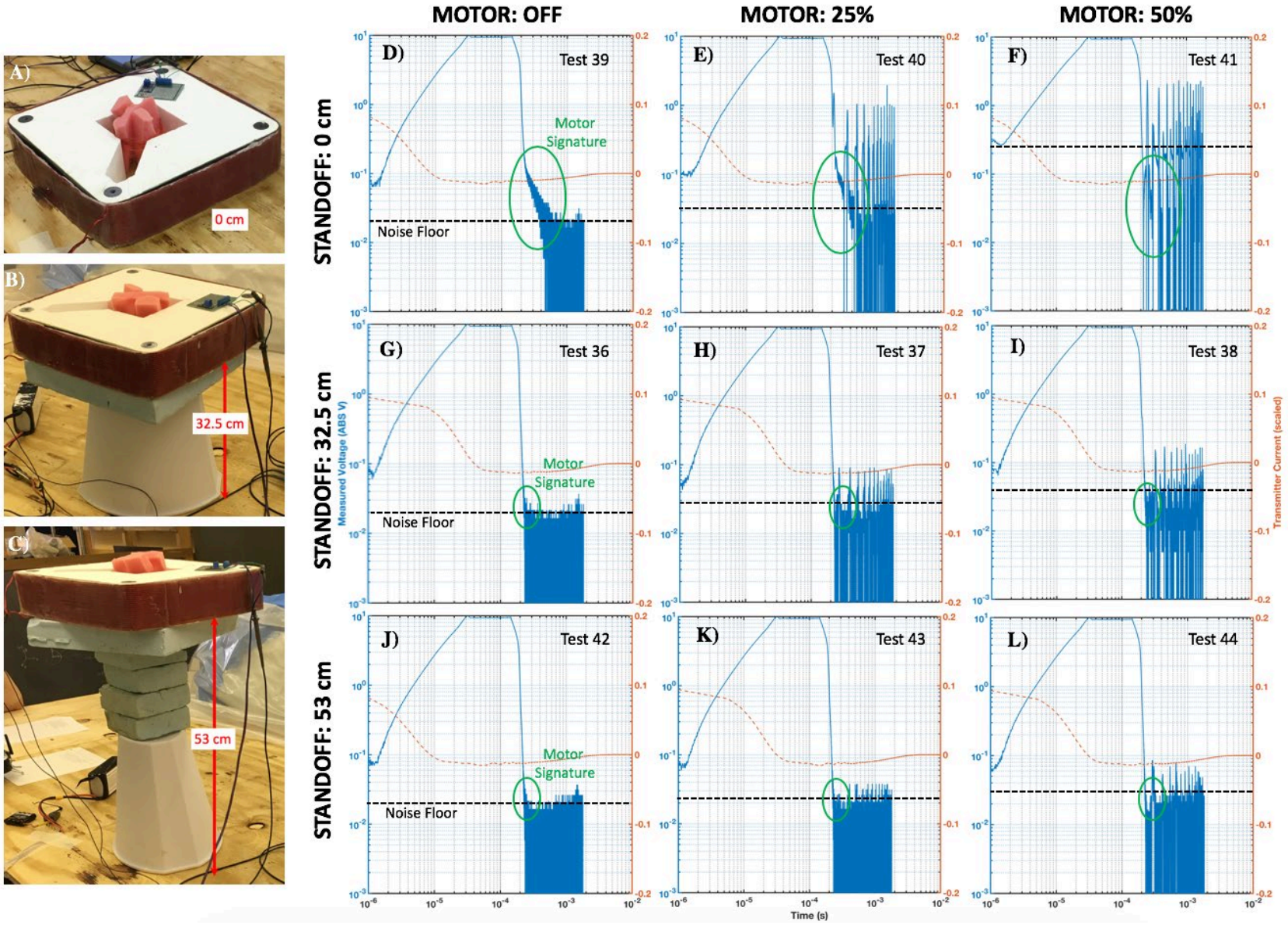

Tests 36–38 represent the same conditions with a standoff distance of 32.5 cm. In this set, the inductive response of the motor is lessened considerably due to the increased distance, and is not observed outside of the noise envelope when the motors are operational. Finally, Tests 42–44 are at a standoff distance of 53 cm. Here the SNR is increased due to the reduction in noise as a result of the increased standoff distance. In each of the cases, the noise resulting from operation of the motor appears to be regularly spaced around 8 kHz. At 50% power and at the greatest distance tested, there's an approximate SNR of 20–30 dB.

4.6 Carbon fiber frame response (Test 45)

Test 45 investigated the response of two types of 1.2 m length carbon fiber angled stock, gathered as a single bundle, as described in section 3.4. As noted in section 3.4, no data were recorded for this simple observation; however, no response was observed on the display.

Most likely, the lack of response for this carbon fiber target, even though we see some response from larger carbon fiber targets such as a 7.5 cm carbon fiber sphere, is that these carbon fiber elements are thin and long and so do not have enough bulk to develop low-frequency (frequency domain) or later time (time-domain) EMI responses that we would measure.

5 Conclusions and Future Work

This preliminary investigation was designed to assess the effects of UAS componentry, specifically propeller motors, on time-domain electromagnetic induction sensors. Additionally, we were able to demonstrate qualitatively that there was no electromagnetic signature associated with the planned carbon-fiber sensor-framing material.

The results of the study indicated that a significant EMI influence could be observed at a standoff distance of 0 cm and 32.5 cm while a negligible influence for a single motor could be observed at a distance of 53 cm. Moving forward, we will consider a distance of 60 cm as sufficient to address the interference concerns associated with a single UAS motor.

Further considerations for development of this EMI sensor will include the fully assembled UAS system with all operating components, including motors, remote system controls, and remote transmission of data. Ultimately, this study provides the foundational knowledge needed to design the prototype UAV based EMI sensor with planned applications for runway UXO detection and permafrost mapping.

References

Auken, E., A. V. Christiansen, C. Kirkegaard, G. Fiandaca, C. Schamper, A. A. Behroozmand, A. Binley, E. Nielsen, F. Effersø, N. B. Christensen, K. Sørensen, N. Foged, and G. Vignoli. 2015. "An Overview of a Highly Versatile Forward and Stable Inverse Algorithm for Airborne, Ground-Based and Borehole Electromagnetic and Electric Data." *Exploration Geophysics* 46 (3): 223–235.

Barrowes, B. E., and T. A. Douglas. 2016. *Evaluation of Electromagnetic Induction (EMI) Resistivity Technologies for Assessing Permafrost Geomorphologies*. ERDC/CRREL TR-16-12. Hanover, NH: U.S. Army Engineer Research and Development Center.

Barrowes, B. E., F. Shubitidze, T. M. Grzegorczyk, J. P. Fernández, and K. O'Neill. 2013. "The Pedemis Instrument: Positioning, Background Subtraction, and APG Field Results." In *Proceedings of SPIE 8709, Detection and Sensing of Mines, Explosive Objects, and Obscured Targets XVIII*.

Barrowes, B. E., J. P. Fernandez, K. O'Neill, I. Shamatava, and F. Shubitidze. 2015. "Electromagnetic Induction Tools for Discrimination of Unexploded Ordnance: From Basic Physics to Blind Tests." *FastTIMES* 20 (1): 13–30.

Barrowes, B. E., J. B. Sigman, Y. Wang, K. O'Neill, F. Shubitidze, J. E. Simms, H. H. Bennett Jr., and D. E. Yule. 2016. "Carbon Fiber and Void Detection Using High-Frequency Electromagnetic Induction Techniques." In *Proceedings of SPIE 9823, Detection and Sensing of Mines, Explosive Objects, and Obscured Targets XXI*. https://doi.org/10.1117/12.2224584.

Barrowes, B. E., F. Shubitidze, J. Sigman, J. Bennett, J. Simms, D. Yule, and K. O'Neill. 2017. "Void and Landmine Detection Using the HFEMI Sensor." In *Proceedings of SPIE 10182, Detection of Sensing of Mines, Explosive Objects, and Obscured Targets XXII*, 10182. https://doi.org/10.1117/12.2262619.

Barrowes, B. E., D. R. Glaser, M. Prishvin, K. O'Neill, and F. Shubitidze. 2018. "Short and Long Wire Detection Using High-Frequency Electromagnetic Induction Techniques." In *Proceedings of SPIE 10628, Detection and Sensing of Mines, Explosive Objects, and Obscured Targets XXIII*.

Bell, R. 2017a. "A Review of UAS Magnetometers." In *Proceedings of the Society of Exploration Geophysics*, 24–29 September, Huston, TX.

Bell, R. 2017b. "Comparison of Ground Magnetic and Low Altitude Aeromagnetic Data." In *Proceedings of the Society of Exploration Geophysics*, 24–29 September, Huston, TX.

Bell, R. 2018a. "Above the Dump: A SUAS Enabled Aeromagnetic Survey of a Landfill." In *Proceedings of the Symposium on the Application of Geophysics for Environmental and Engineering Problems SAGEEP*, 25–29 March, Nashville, TN.

Bell, R. 2018b. "Drone Enabled Geoscientific Mapping is the New Paradigm for Environmental Site Characterization." In *Proceedings of the Symposium on the Application of Geophysics for Environmental and Engineering Problems SAGEEP*, 25–29 March, Nashville, TN.

Cheng, D.K. 1989. *Field and Wave Electromagnetics*. 2nd ed. New York: Addison-Wesley.

Eröss, R., B. Tezkan, J. B. Stoll, and R. Bergers. 2017. "Interpretation of Very Low Frequency Measurements Carried Out with an Unmanned Aerial System by 2D Conductivity Models." *Journal of Environmental and Engineering Geophysics* 22 (1): 83–94.

Fernández, J. P., B. E. Barrowes, T. M. Gregorczyk, N. Lhomme, K. A. O'Neill, and F. Shubitidze. 2011. "A Man-Portable Vector Sensor for Identification of Unexploded Ordinance." *IEEE Sensors Journal* 11 (10): 2542–2555.

Glaser, D. R., and A. M. Wagner. 2019. "Dynamic Cold Regions Terrain Effects on Time-Domain Electromagnetic Induction Data." *Cold Regions Science and Technology*, 158:52–61.

Glaser, D. R., A. M. Wagner, A. B. Gelvin, S. Saari, A. Staples, and G. Larsen. 2017. "Snow Depth Calibrations for Electromagnetic Induction Investigations at a Former Munitions Waste Disposal Site in Alaska." Presented at the American Geophysical Union Fall Meeting, 11–15 December, New Orleans, LA.

Glaser, D. R, B. E. Barrowes, K. O'Neill, M. Prishvin, B. G. Quinn, and F. Shubitidze. 2018. "Electromagnetic Induction Measurements of Induced Polarization for Characterization of Near Surface Soils." Presented at the 5th International Workshop on Induced Polarization, 3–5 October, Rutgers University Newark, Newark, NJ.

Grant, S. A., B. E. Barrowes, F. Shubitidze, and S. A. Arcone. 2014. "Homemade Explosives in the Subsurface as Intermediate Electrical Conductivity Materials: A New Physical Principle for Their Detection." In *Proceedings of SPIE 9072, Detection and Sensing of Mines, Explosive Objects, and Obscured Targets XIX*. https://doi.org/10.1117/12.2050430.

Hoekstra, P., P. V. Sellman, and A. Delaney. 1975. "Ground and Airborne Resistivity Surveys of Permafrost Near Fairbanks, Alaska." *Geophysics*, 40 (4): 593–701.

Hoekstra, B., and R. Mhaskar. 2017. "MFAM: Miniature Fabricated Atomic Magnetometer for Autonomous Magnetic Surveys." In *Proceedings of the Society of Exploration Geophysics*, 24–29 September, Huston, TX.

Kang, S. 2018. On Recovering Distributed Induced Polarization Information from Time-Domain Electromagnetic Data. PhD thesis, University of British Columbia. http://hdl.handle.net/2429/64757.

McKenna, S. P., K. B. Parkman, L. J. Perren, and J. R. McKenna. 2013. "Automatic Detection of a Subsurface Wire Using an Electromagnetic Gradiometer." *IEEE Transactions on Geoscience and Remote Sensing* 51 (1): 132–139.

Minsley, B. J., J. D. Abraham, B. D. Smith, J. C. Cannia, C. I. Voss, M. T. Jorgenson, M. A. Walvoord, B. K. Wylie, L. Anderson, L. B. Ball, and M. Deszcz-Pan. 2012. "Airborne Electromagnetic Imaging of Discontinuous Permafrost." *Geophysical Research Letters* 39 (2): L02503.

O'Neill, K. 2016. *Discrimination of Subsurface Unexploded Ordnance*. Tutorial Texts in Optical Engineering, Vol. TT102. Bellingham, WA: SPIE Press.

Pastick, N. J., M. T. Jorgenson, B. K. Wylie, B. J. Minsley, L. Ji, M. A. Walvoord, B. D. Smith, J. D. Abraham, and J. R. Rose. 2013. "Extending Airborne Electromagnetic Surveys for Regional Active Layer and Permafrost Mapping with Remote Sensing and Ancillary Data, Yukon Flats Ecoregion Central Alaska." *Permafrost and Periglacial Processes* 24 (3): 184–199.

Prouty, M., and R. Johnson. 2010. "Small, Low Power, High Performance Magnetometers." In *Proceedings, EGM 2010 International Workshop*, 11–14 April, Capri, Italy. http://www.eageseg.org/data/egm2010/Sessione%20A/Oral%20papers/A_OP_11.pdf.

Seidel, M., and B. Tezkan. 2017. "1D Cole-Cole Inversion of TEM Transients Influenced by Induced Polarization." *Journal of Applied Geophysics* 138:220–232.

SERDP (Strategic Environmental Research and Development Program) and ESTCP (Environmental Security Technology Certification Program). 2016. Classification Applied to Munitions Response. https://www.serdp-estcp.org/Featured-Initiatives/Munitions-Response-Initiatives/Classification-Applied-to-Munitions-Response.

Shubitidze, F., B. Barrowes, J. Sigman, Y. Wang, I. Shamatava, and K. O'Neill. 2014a. "Detecting and Classifying Small and Deep Targets Using Improved EMI Hardware and Data Processing Approach." In *Proceedings of SPIE 9072, Detection and Sensing of Mines, Explosive Objects, and Obscured Targets XIX*.

Shubitidze, F., J. Sigman, K. O'Neill, I. Shamatava, and B. Barrowes. 2014b. "High Frequency Electromagnetic Induction Sensing for Non-Metallic Ordnances Detection." In *Proceedings of the International Seminar/Workshop on Direct and Inverse Problems of Electromagnetic and Acoustic Wave Theory (DIPED)*, 180–182.

Shubitidze, F., B. Barrowes, J. B. Sigman, J. Simms, J. Bennett, D. Yule, I. Shamatava, and K. O'Neill. 2016a. "Detection and Discrimination Subsurface Low Conducting Buried Hazards in a Cluttered Environment." Presented at the Symposium on the Application of Geophysics to Engineering and Environmental Problems, 20–24 March, Denver, CO.

Shubitidze, F., B. E. Barrowes, J. B. Sigman, K. O'Neill, and I. Shamatava. 2016b. "UXO Classification Procedures Applied to Advanced EMI Sensors and Models." In *Proceedings of the International Seminar/Workshop on Direct and Inverse Problems of Electromagnetic and Acoustic Wave Theory (DIPED)*, 173–177.

Sigman, J. B., Barrowes, B. E., Wang, Y., Bennett, H. J., Simms, J. E., Yule, D. E., O'Neill, K., and F. Shubitidze. 2017a. "Coil Design Considerations for a High-Frequency Electromagnetic Induction Sensing Instrument." In Proceedings of SPIE—The International Society for Optical Engineering, 9–13 April, Anaheim, CA.

Sigman, J. B., B. E. Barrowes, K. O'Neill, Y. Wang, J. E. Simms, H. H. Bennett Jr., D. E. Yule, and F. Shubitidze. 2017b. "High-Frequency Electromagnetic Induction Sensing of Non-Metallic Materials." *IEEE Transactions on Geoscience and Remote Sensing* 55 (9): 5254–5263.

Simms, J. E., J. B. Sigman, B. E. Barrowes, H. H. Bennett Jr., D. E. Yule, K. O'Neill, and F. Shubitidze. 2017. "Initial Development of a High-Frequency EMI Sensor for Detection of Subsurface Intermediate Electrically Conductive (IEC) Targets." *Journal of Environmental and Engineering Geophysics* 22 (2): 111–120.

Smith, R. S., and G. F. West. 1989. "Field Examples of Negative Coincident Loop Transient Electromagnetic Responses Modeled with Polarizable Halfplanes." *Geophysics* 54 (11): 1491–1498.

Wait, J. R. 1951. "A Conducting Sphere in a Time Varying Magnetic Field." *Geophysics* 16:666–672.

Appendix A: TDEMI DATA

Here we present the raw TDEMI data measured during this test. In most cases, data are plotted on a log-log scale to demonstrate the responses relative to the noise envelope and motor interference. For all of the log-log plots, the absolute value of the data was calculated prior to plotting to represent all of the data on the plot. In some cases, a linear timescale plot is provided to better visualize the cyclical response of the rotating motors. Test conditions for each output below are indicated in detail in Table 1 and are summarized in each description below. Note that the data files for Tests 8, 24, and 34 were irretrievably corrupted, leaving only the screen captures from the experiment to provide in this section. Also note that Test 45, as described in section 3, was a qualitative assessment with no recorded data. The primary y-axis presents the absolute value of the measured voltage (ABS V).

Figure A-1. Test 1. Initial background test. Amplifier error and troubleshooting.

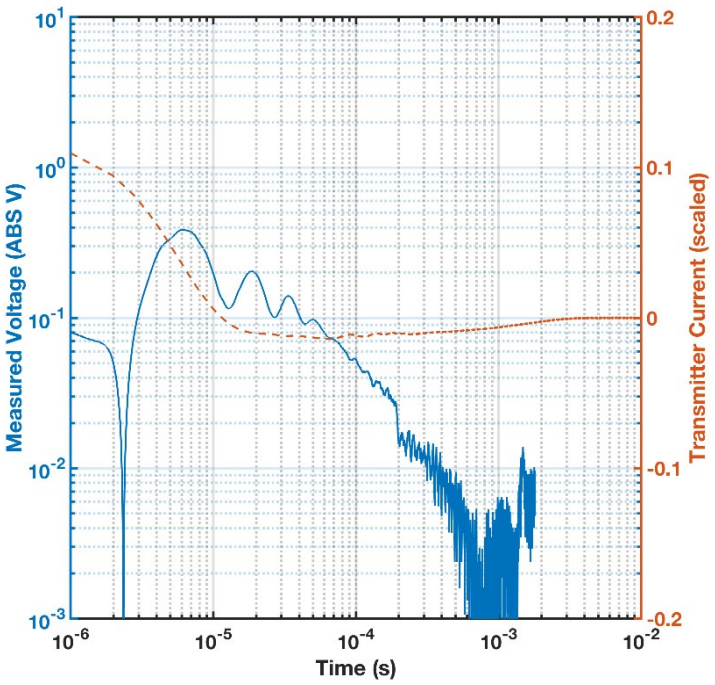

Figure A-2. Test 2. Amplifier error and troubleshooting.

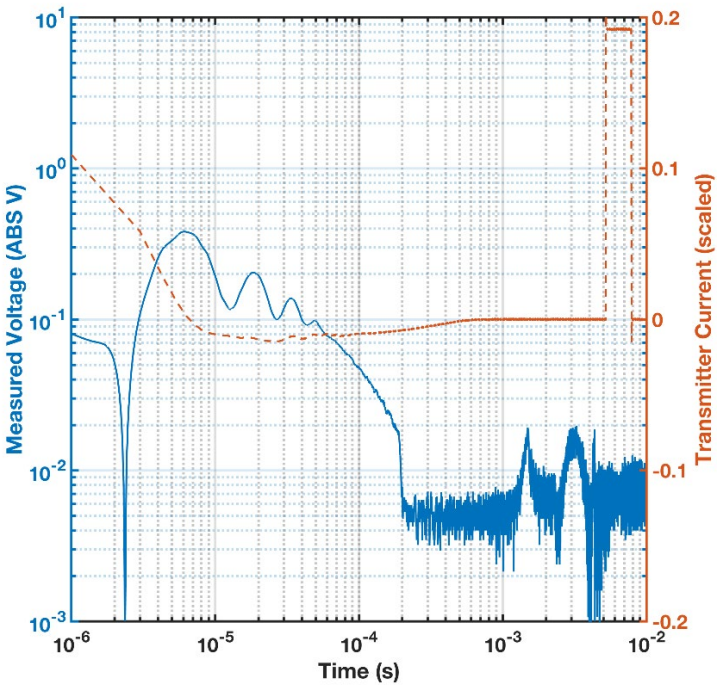

Figure A-3. Test 3. Amplifier error and troubleshooting.

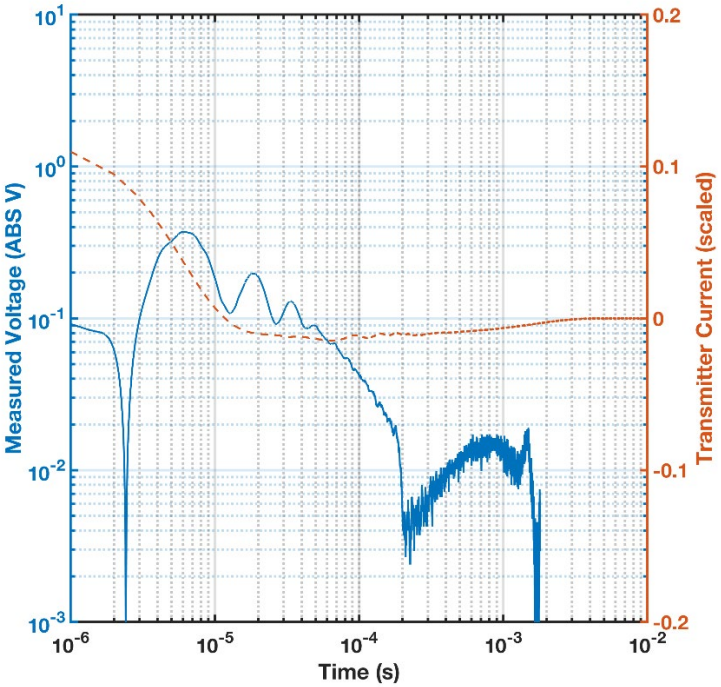

Figure A-4. Test 4. Three periods of testing, linear time scale, background conditions.

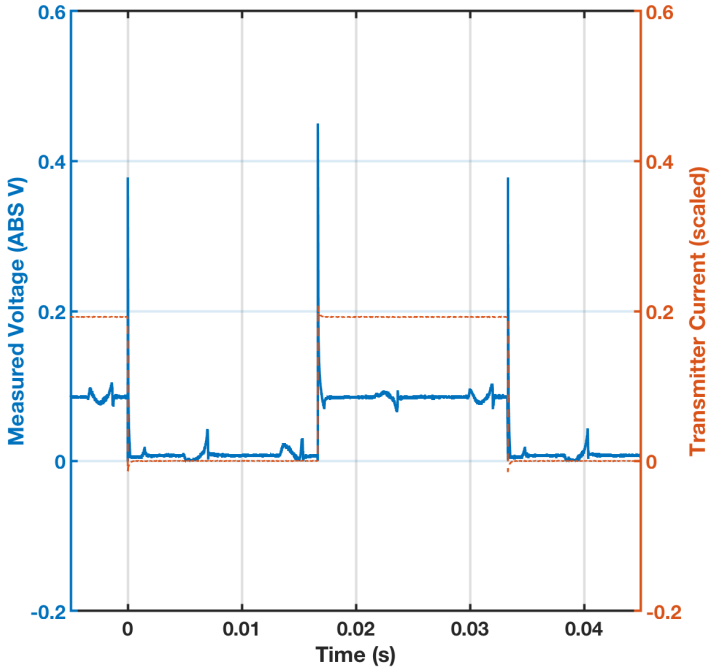

Figure A-5. Test 5. Amplifier error and troubleshooting.

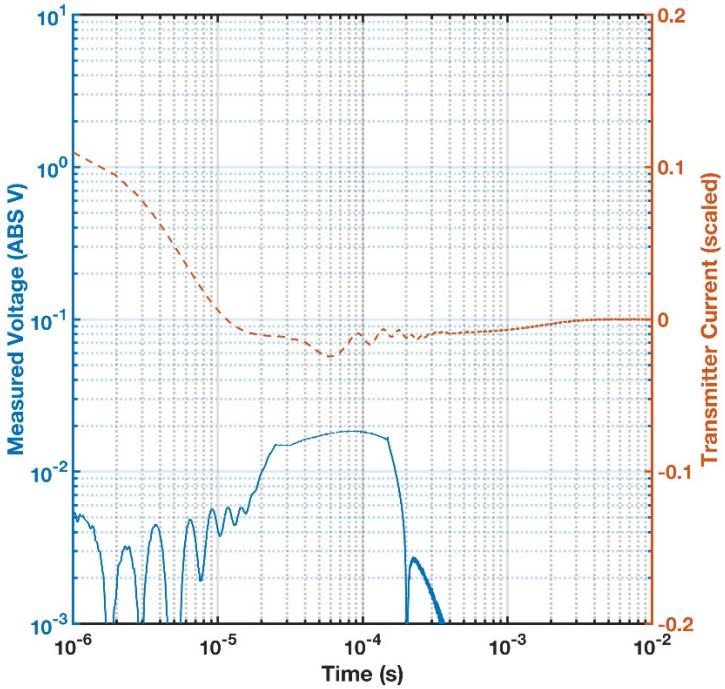

Figure A-6. Test 6. First official background. Systems operations functioning as designed. Motor present at 0 cm offset and in the off configuration.

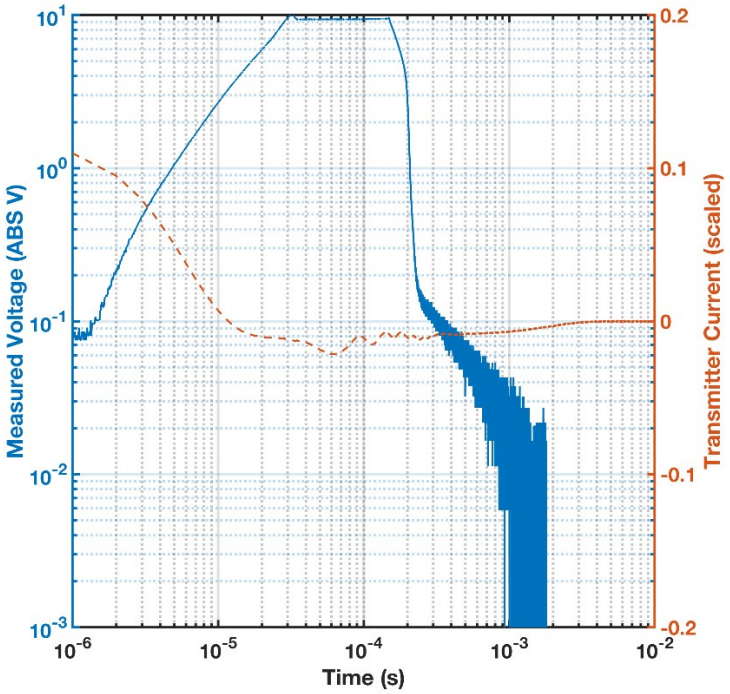

Figure A-7. Test 7. 1.5 periods, linear scale.

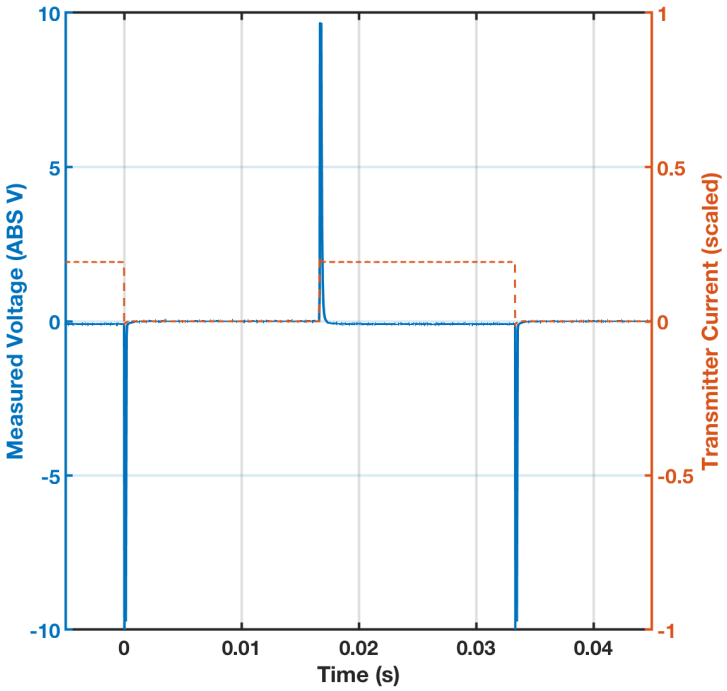

Figure A-8. Test 8 (data file irretrievably corrupted). Background.

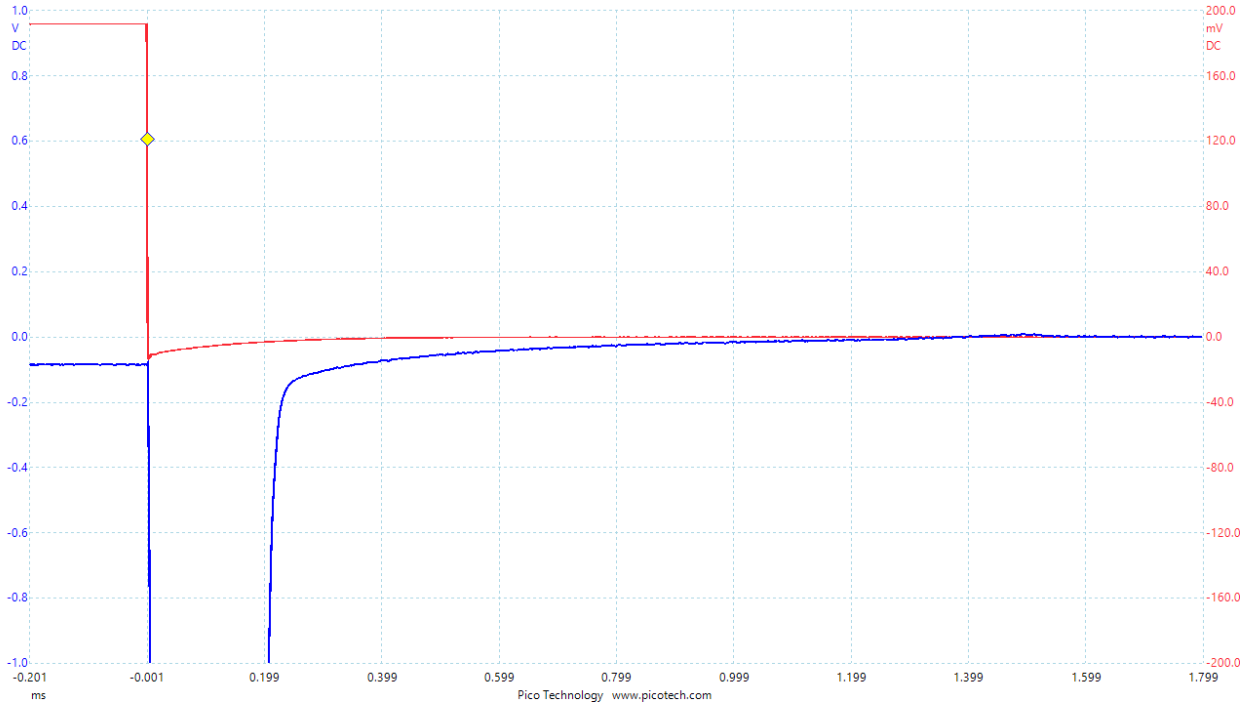

Figure A-9. Test 9. Steel target, 0 cm offset, motor off.

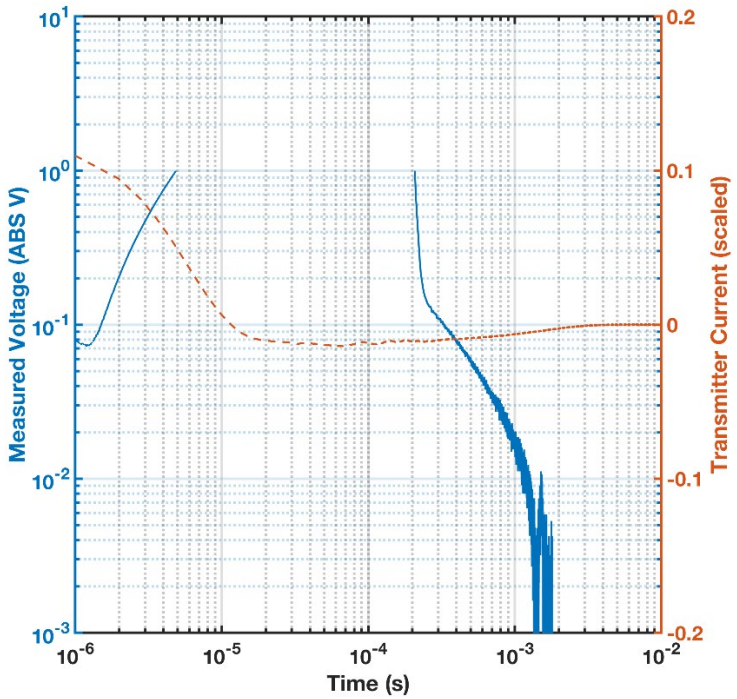

Figure A-10. Test 10. Repeat, steel cylinder.

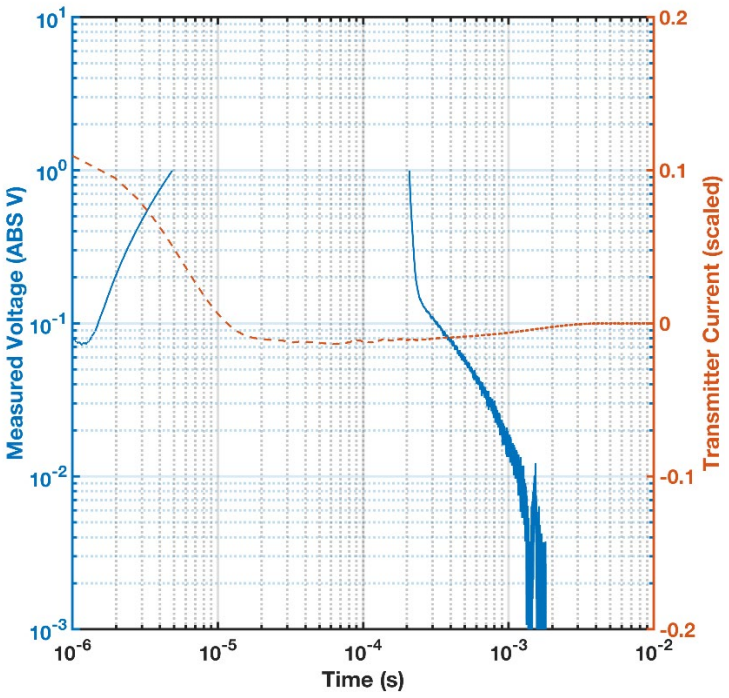

Figure A-11. Test 11. A 40 mm target, 0 cm offset.

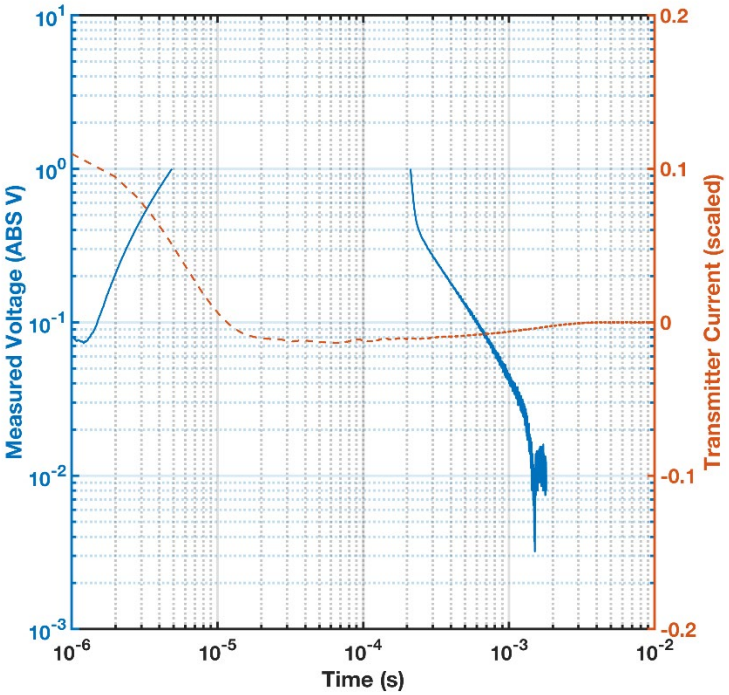

Figure A-12. Test 12. Linear and log-log presentation. Note battery and motor signal.

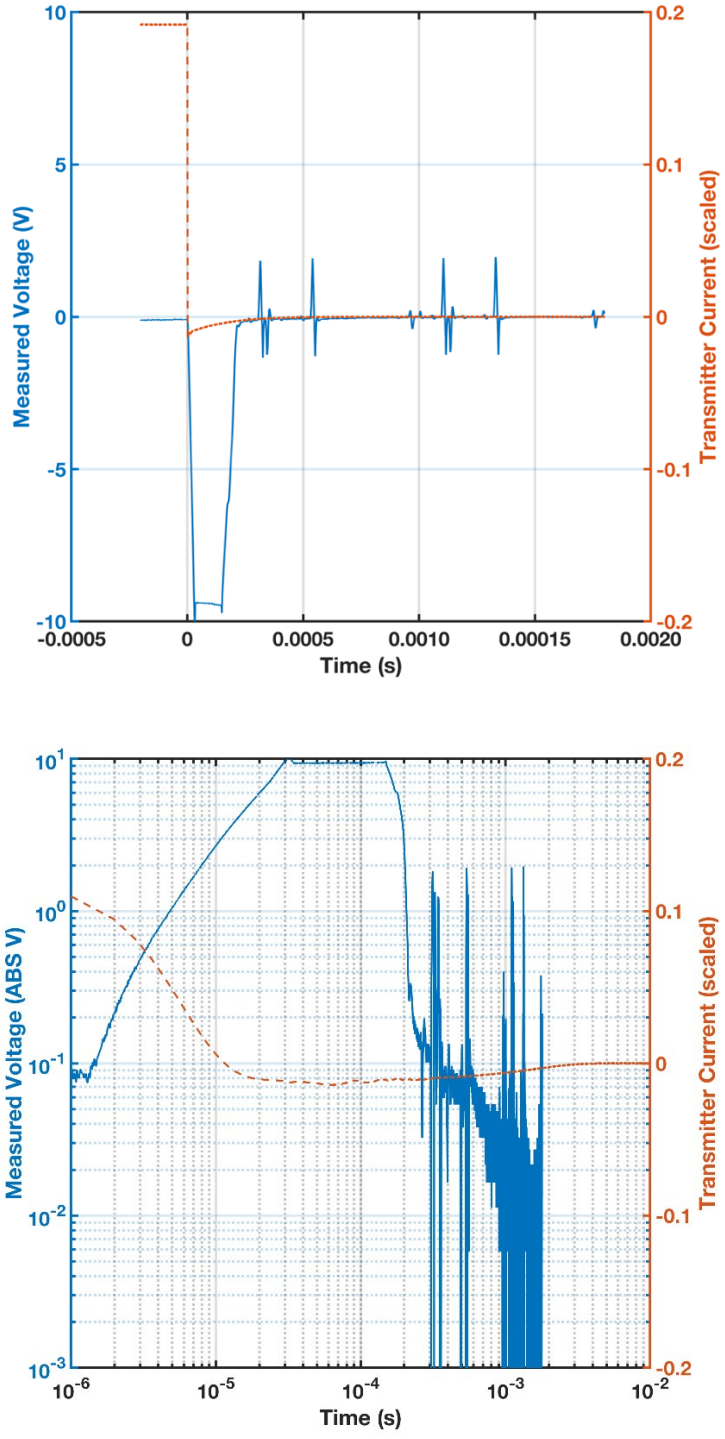

Figure A-13. Test 13. Linear and log-log presentation.
Propellers attached, new motor, 0 cm offset, 25% duty cycle.

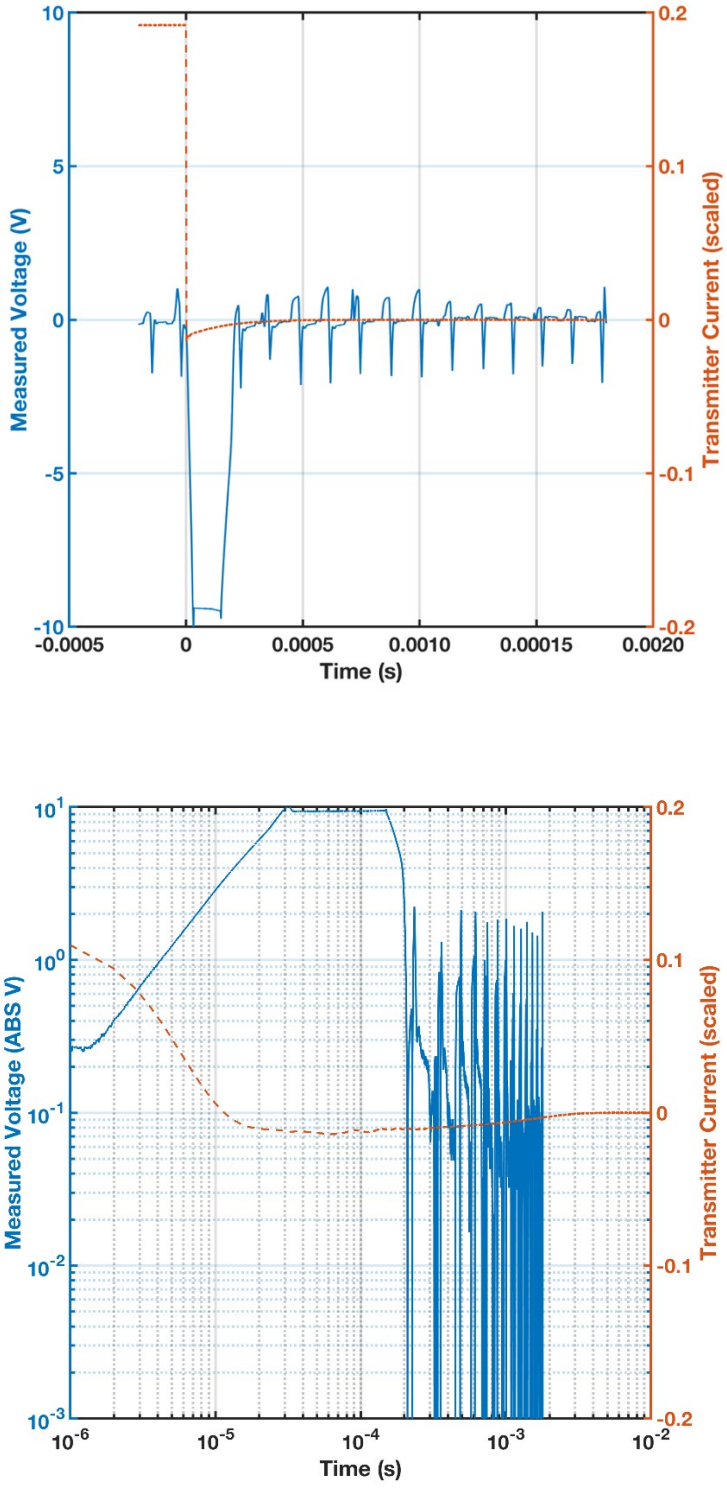

Figure A-14. Test 14. Linear and log-log presentation.
Propellers attached, new motor, 0 cm offset, 50% duty cycle.

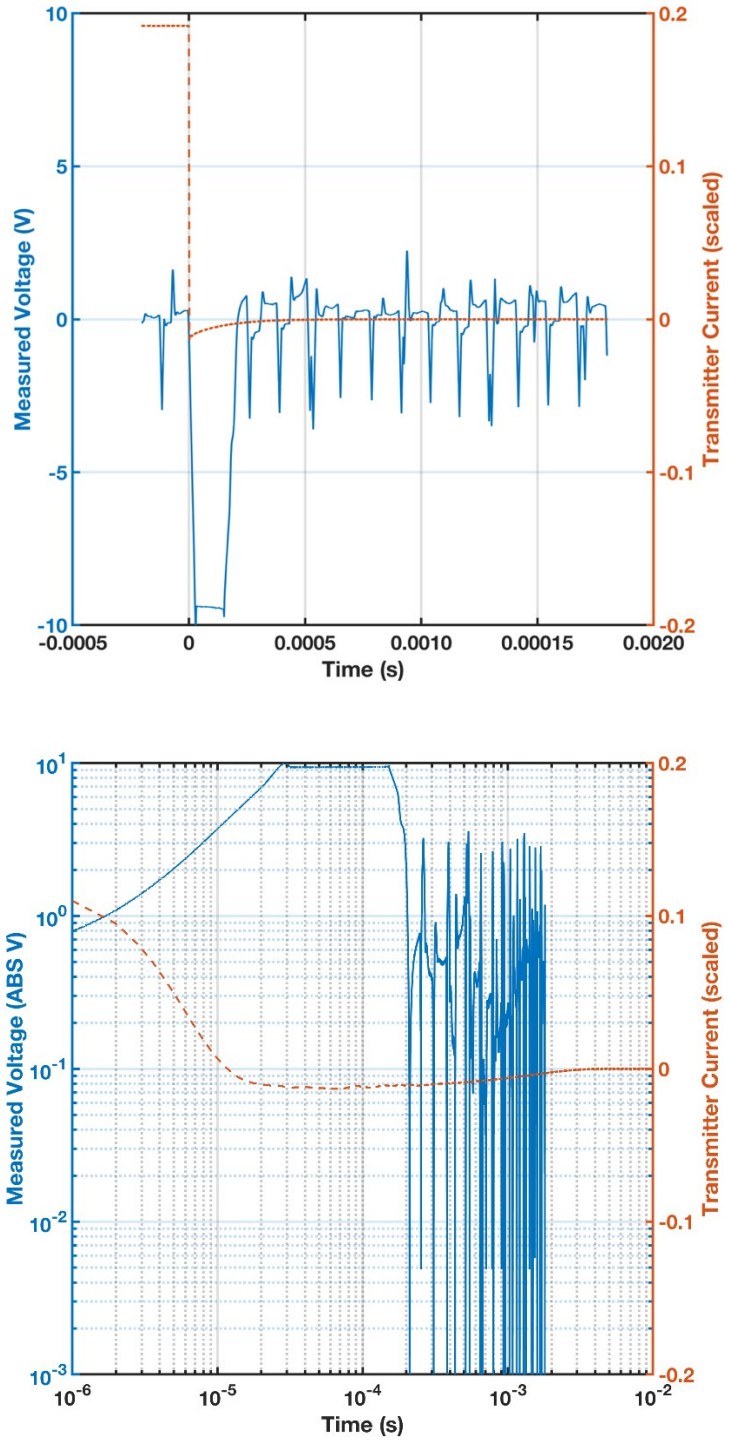

Figure A-15. Test 15. Linear and log-log presentation.
Propellers attached, new motor, 32.5 cm offset, motor off.

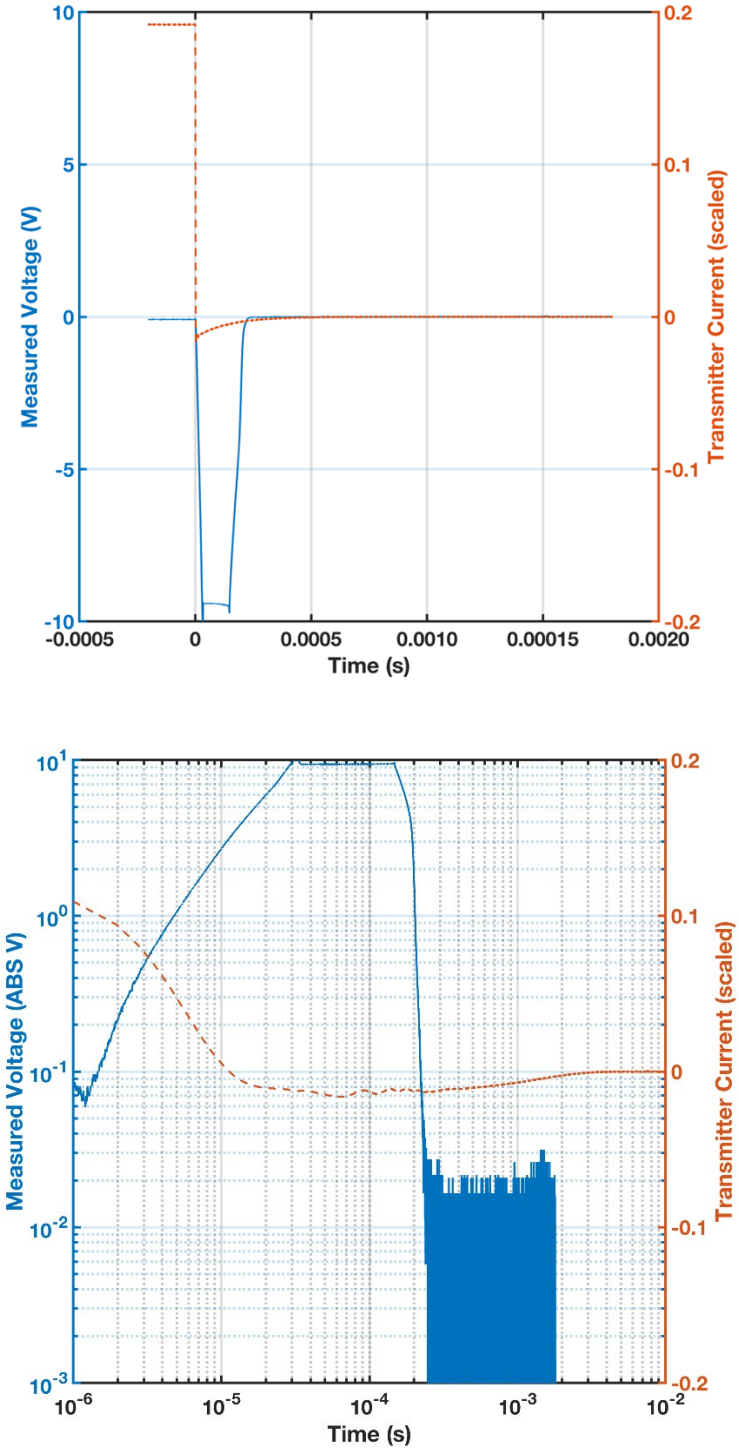

Figure A-16. Test 16. Linear and log-log presentation.
Propellers attached, new motor, 32.5 cm offset, 25% duty cycle.

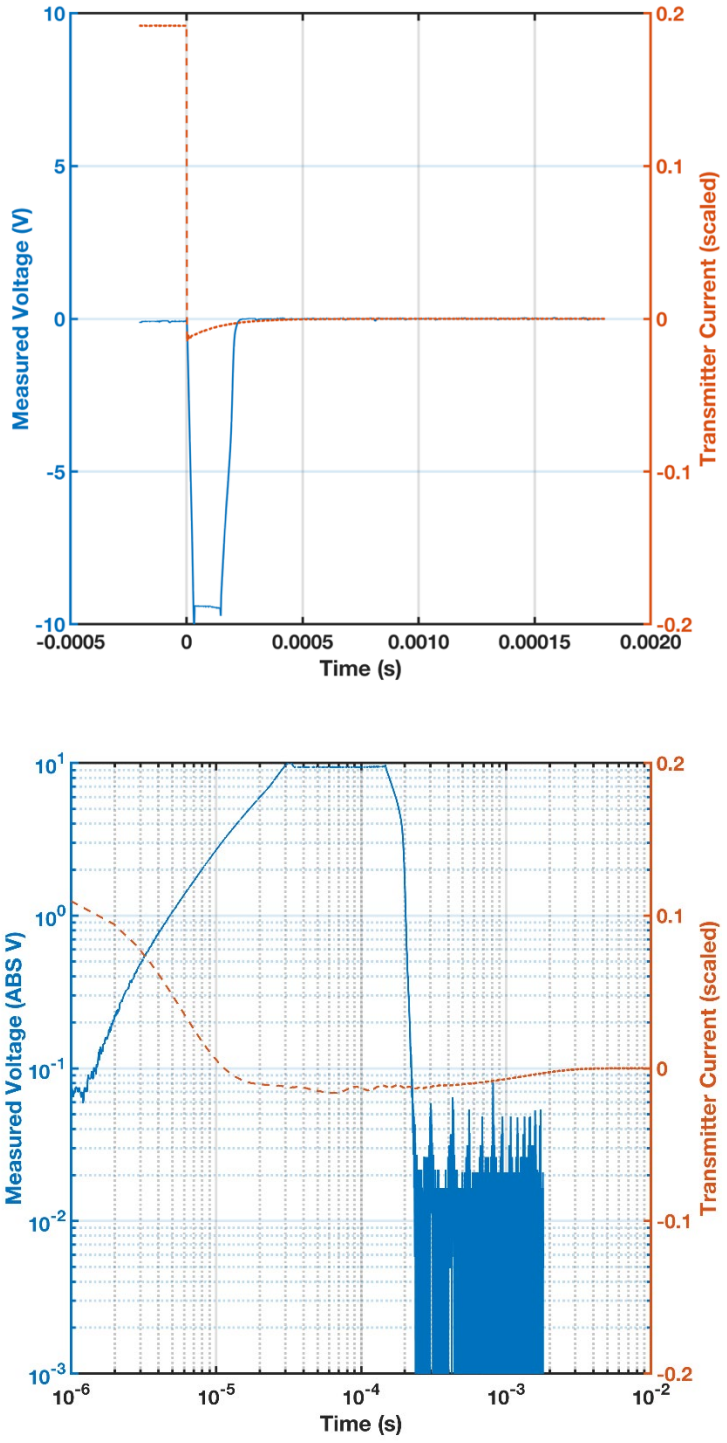

Figure A-17. Test 17. Linear and log-log presentation.
Propellers attached, new motor, 32.5 cm offset, 50% duty cycle.

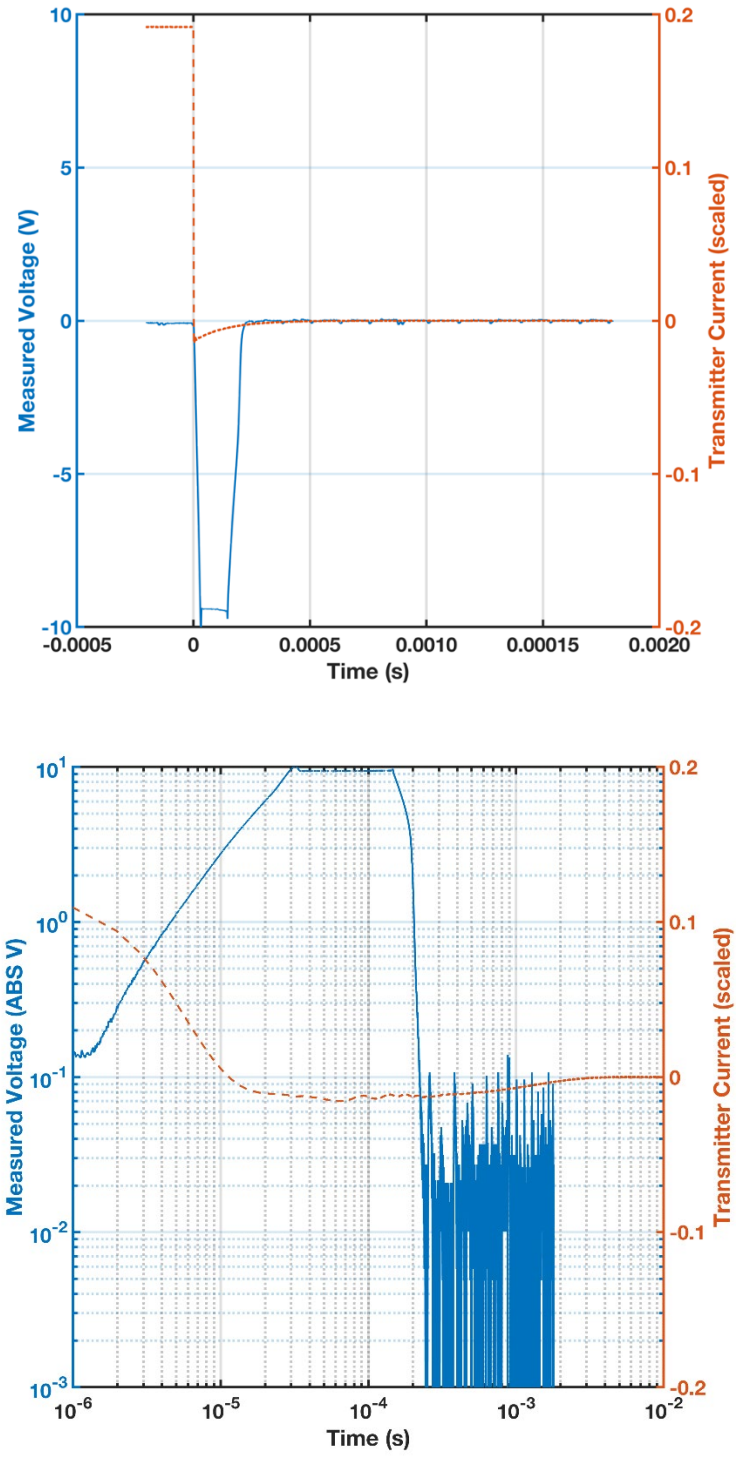

Figure A-18. Test 18. Frequency-domain 12 Hz–500 kHz, 32.5 cm offset, motor off, old motor.

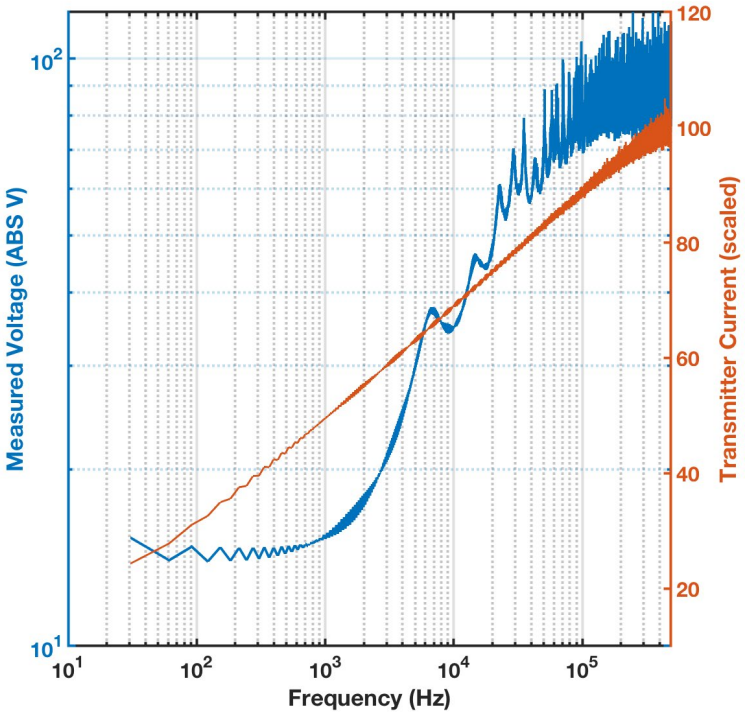

Figure A-19. Test 19. Frequency-domain 12 Hz–500 kHz, 32.5 cm offset, motor 25%, old motor.

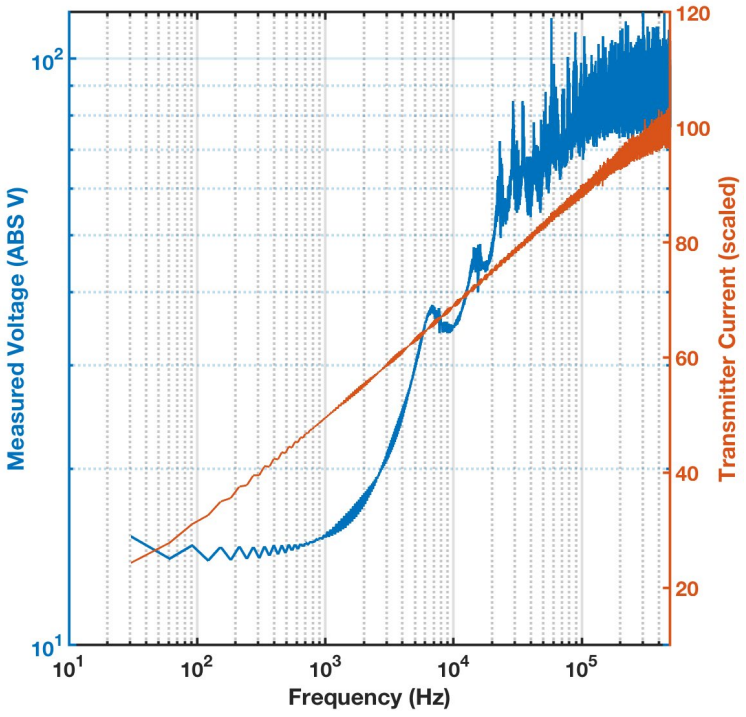

Figure A-20. Test 20. Frequency-domain 12 Hz–500 kHz, 32.5 cm offset, motor 50%.

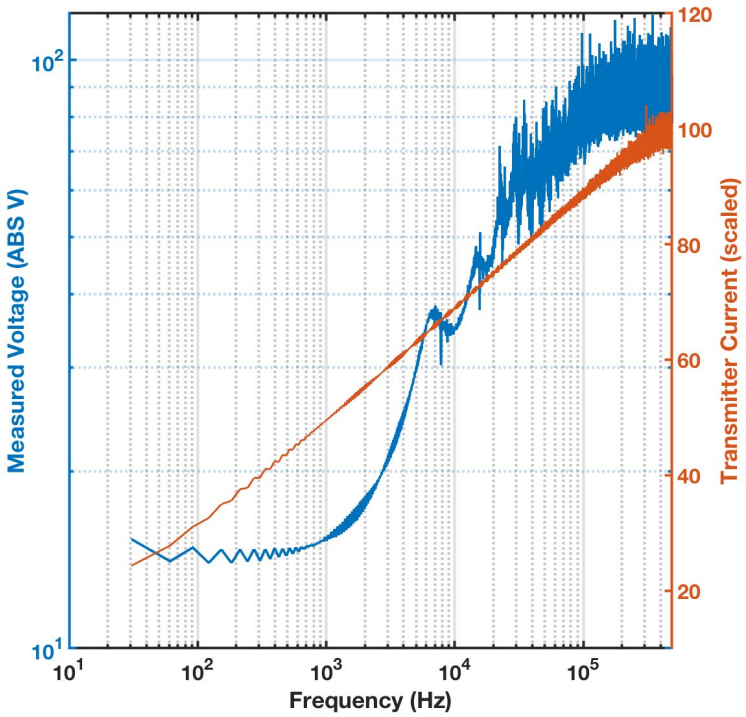

Figure A-21. Test 21. Linear and log-log presentation. No motor present, 32.5 cm offset.

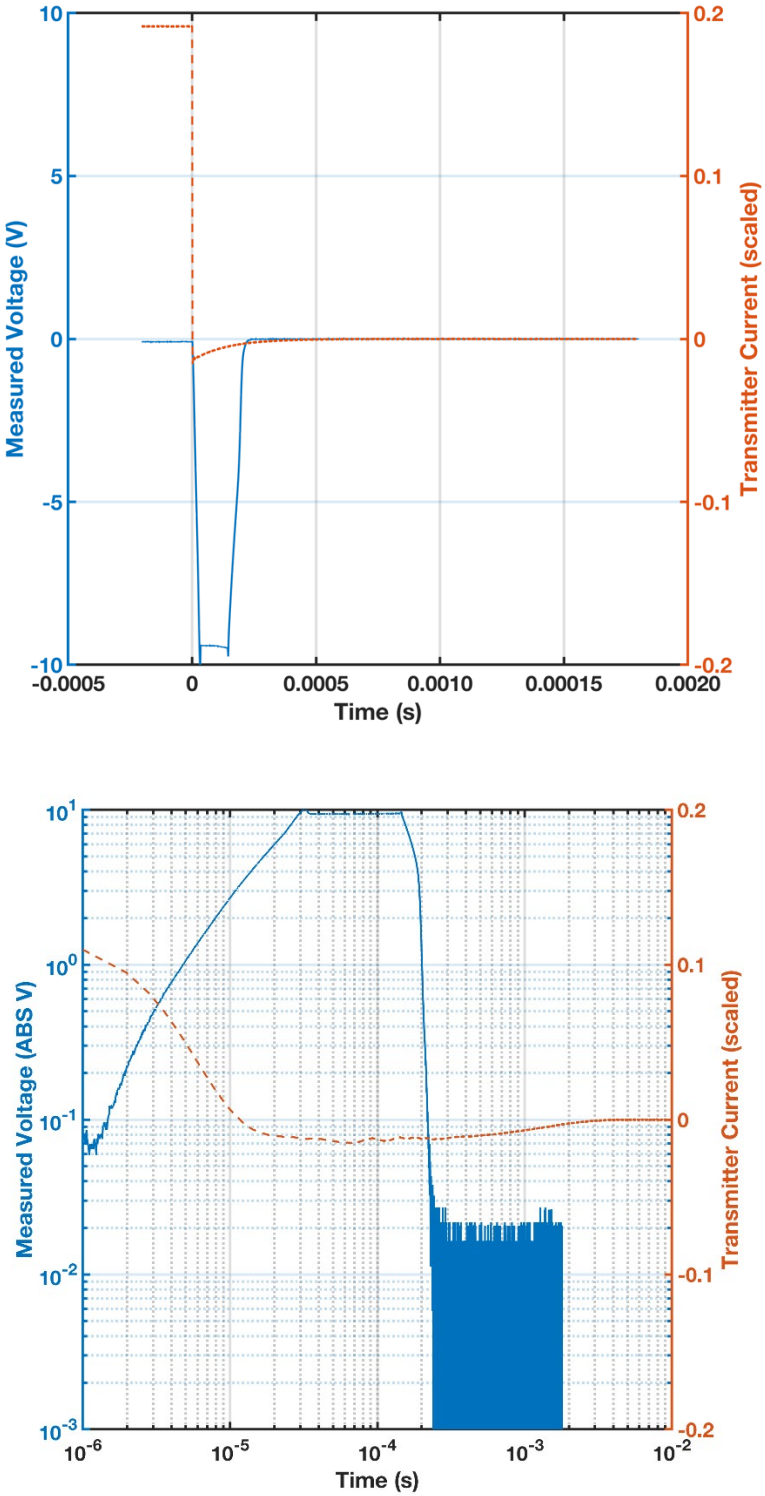

Figure A-22. Test 22. Linear and log-log presentation. No motor present, 32.5 cm offset. 40 mm target present at 5 cm from the Rx sensor.

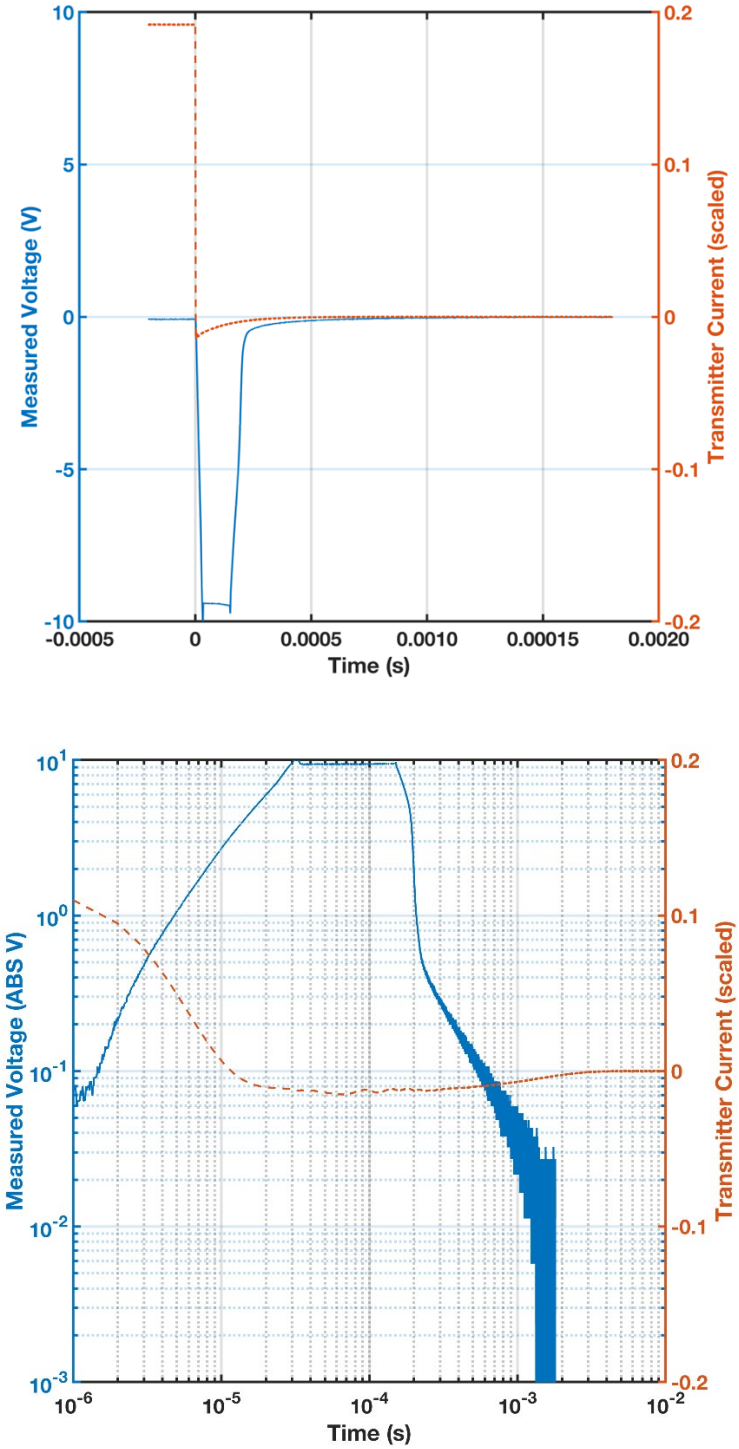

Figure A-23. Test 23. Linear and log-log presentation. New motor, on 25%, 32.5 cm offset, 40 mm target present at 5 cm from the Rx sensor.

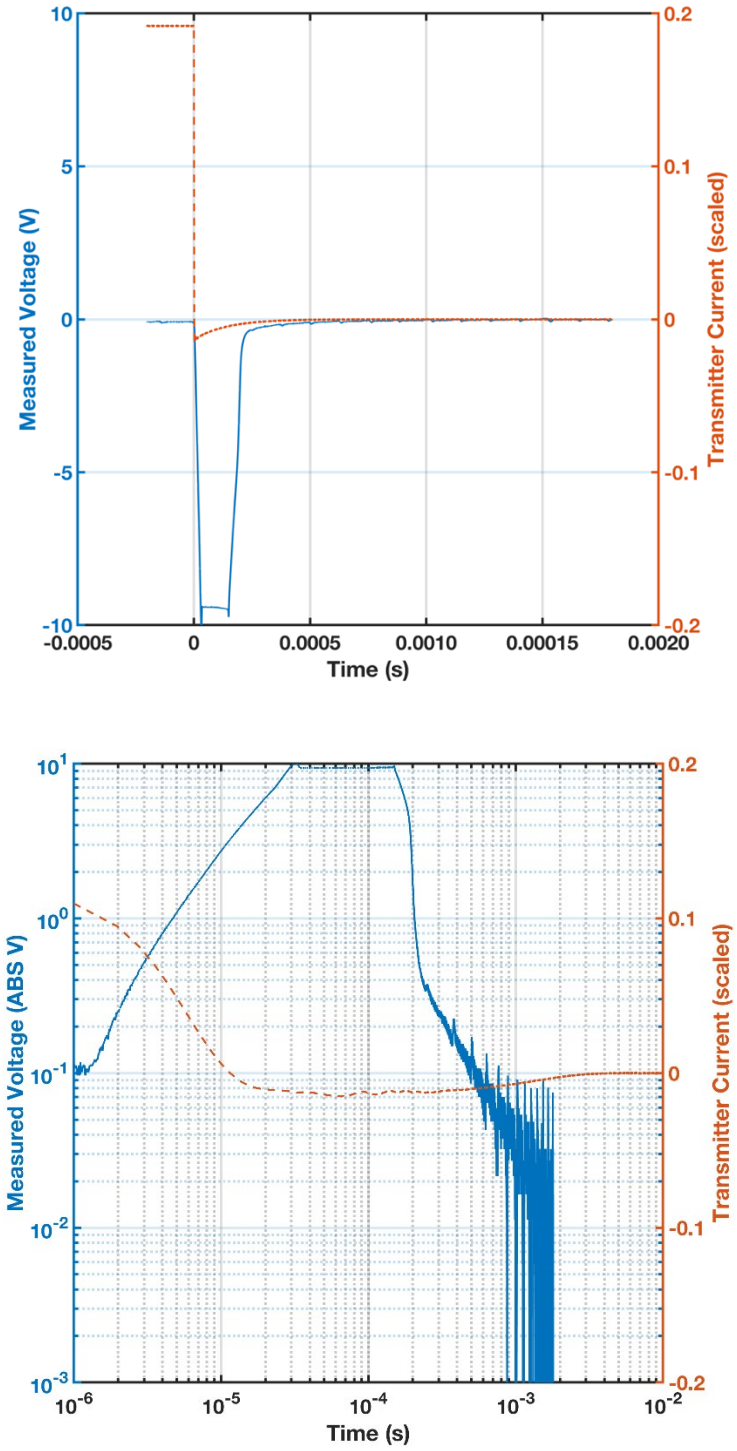

Figure A-24. Test 24 (data file irretrievably corrupted). Linear and log-log presentation. New motor, on 50%, 32.5 cm offset, 40 mm target present at 5 cm from the Rx sensor.

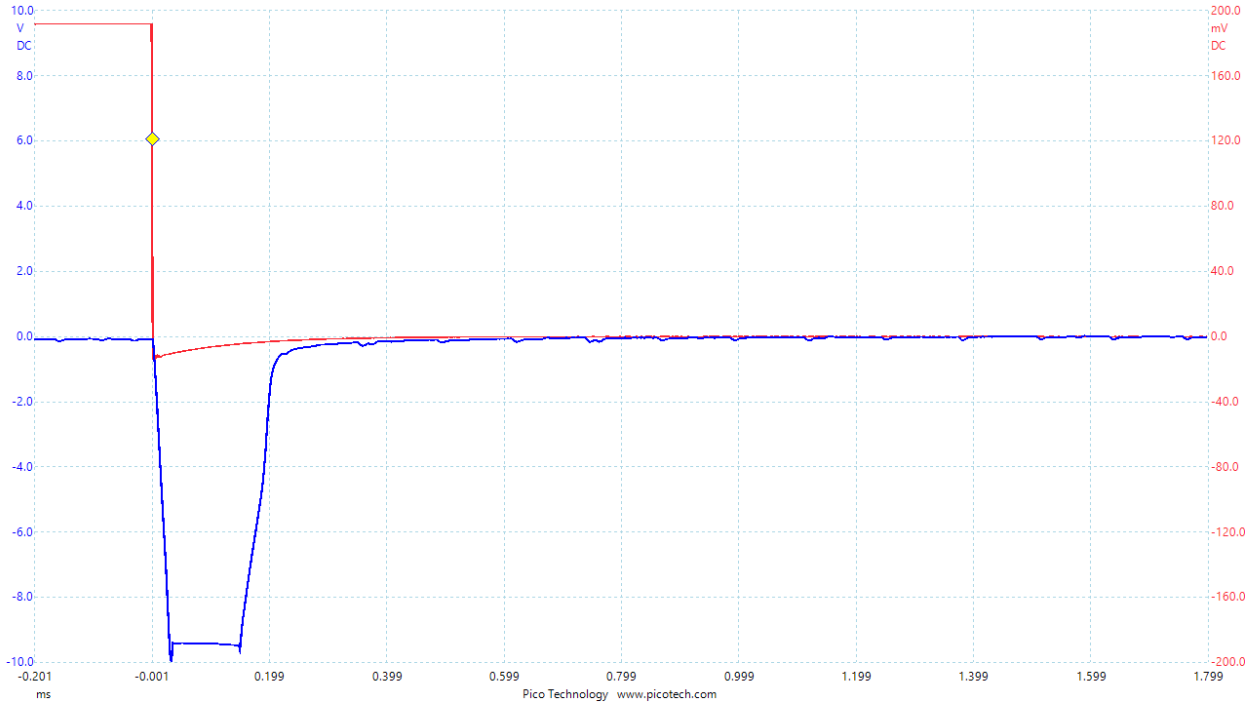

Figure A-25. Test 25. Repeat of test 23.

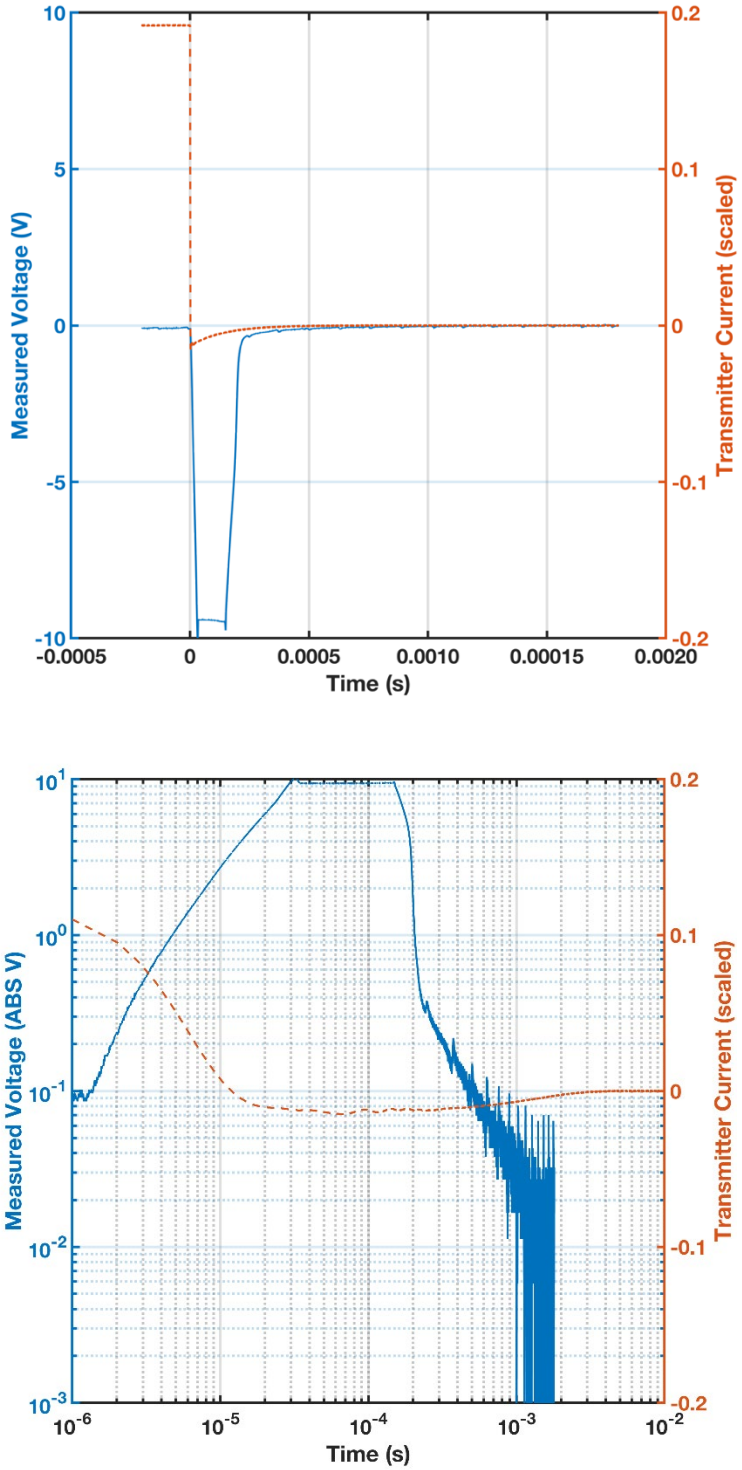

Figure A-26. Test 26. Linear and log-log presentation. New motor, no propellers, on 25%, 32.5 cm offset, no target.

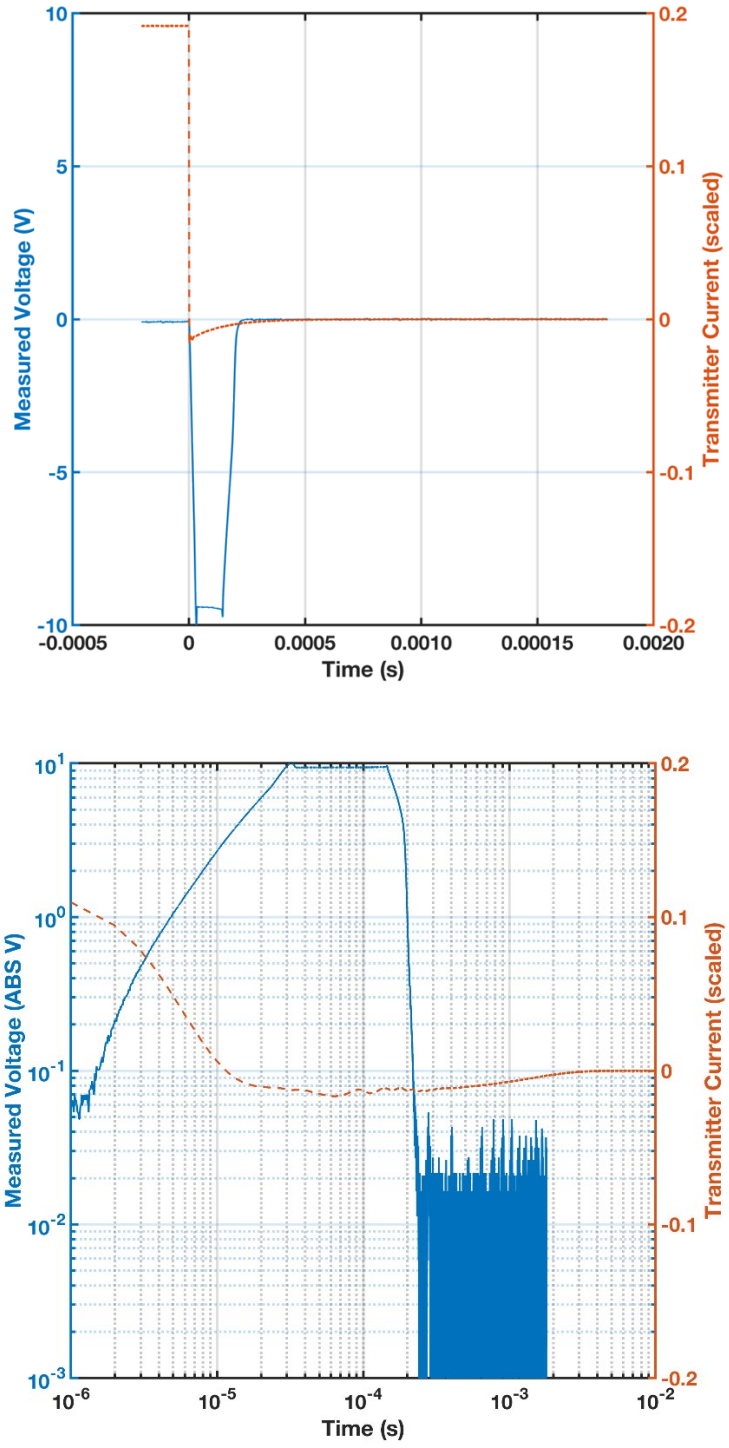

Figure A-27. Test 27. Linear and log-log presentation. New motor, no propellers, on 50%, 32.5 cm offset, no target.

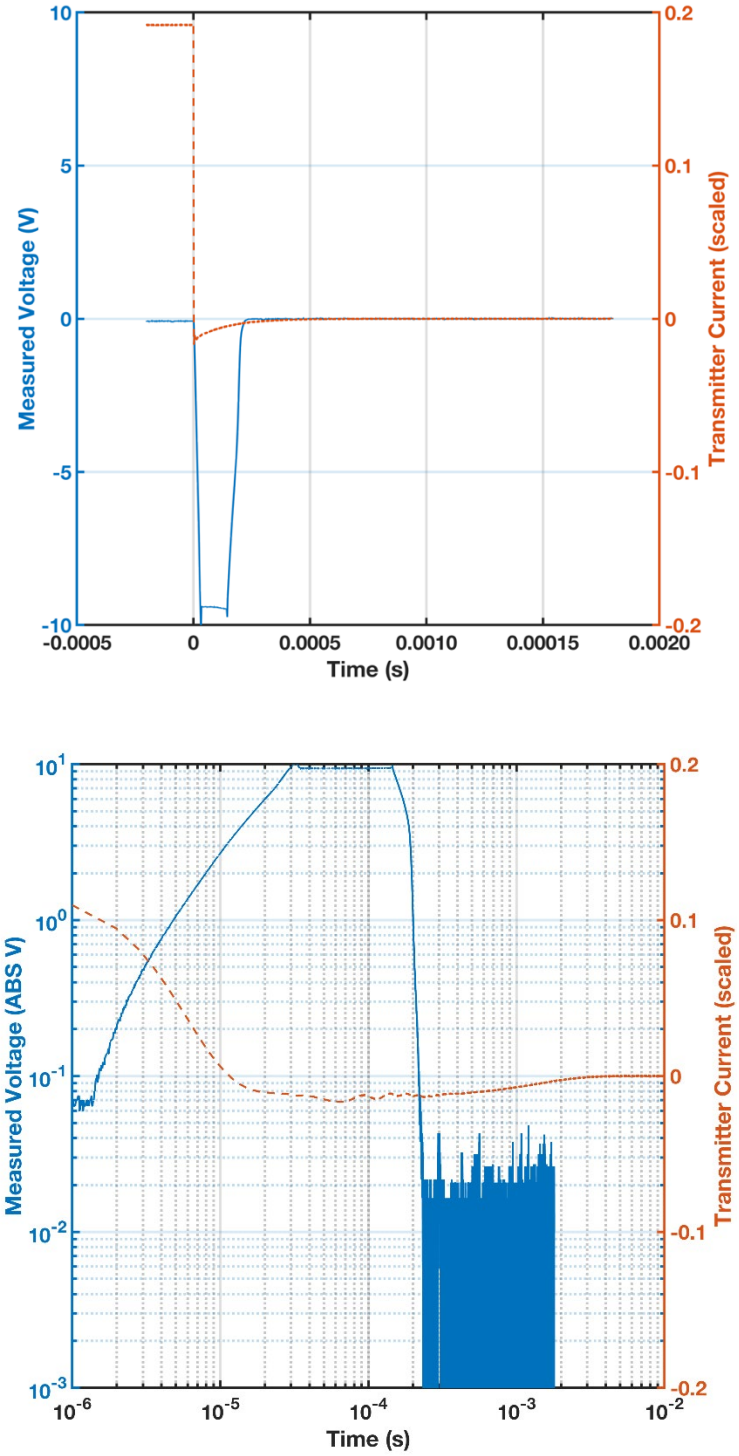

Figure A-28. Test 28. Frequency-domain 12 Hz–500 kHz, 32.5 cm offset, new motor, motor 25%.

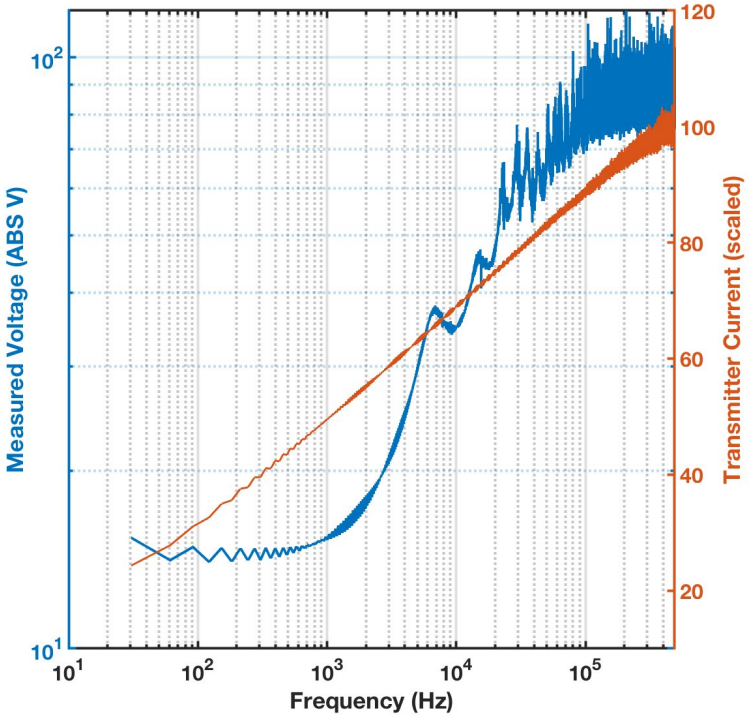

Figure A-29. Test 29. Frequency-domain 12 Hz–500 kHz, 32.5 cm offset, new motor, motor 50%.

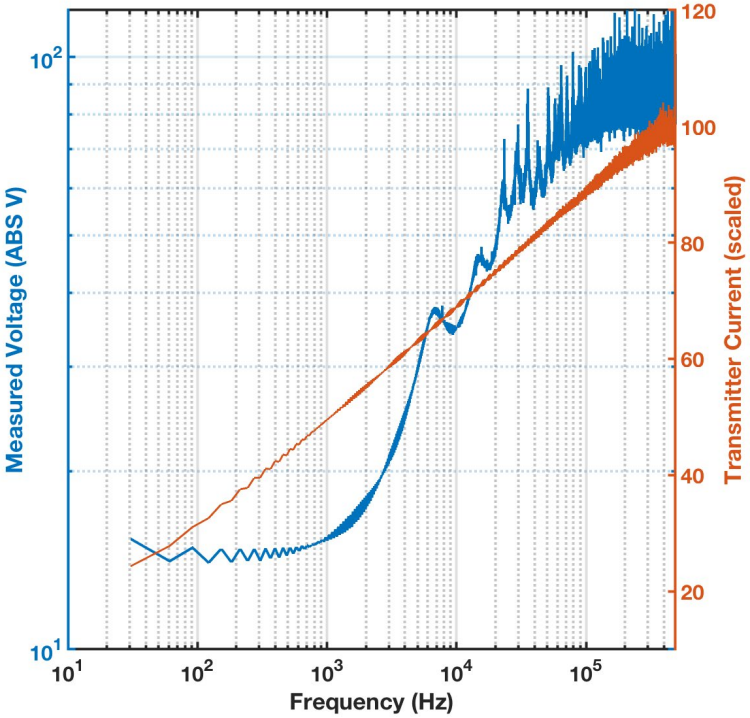

Figure A-30. Test 30. Linear and log-log presentation. Old motor, no propellers, off, 32.5 cm offset, no target.

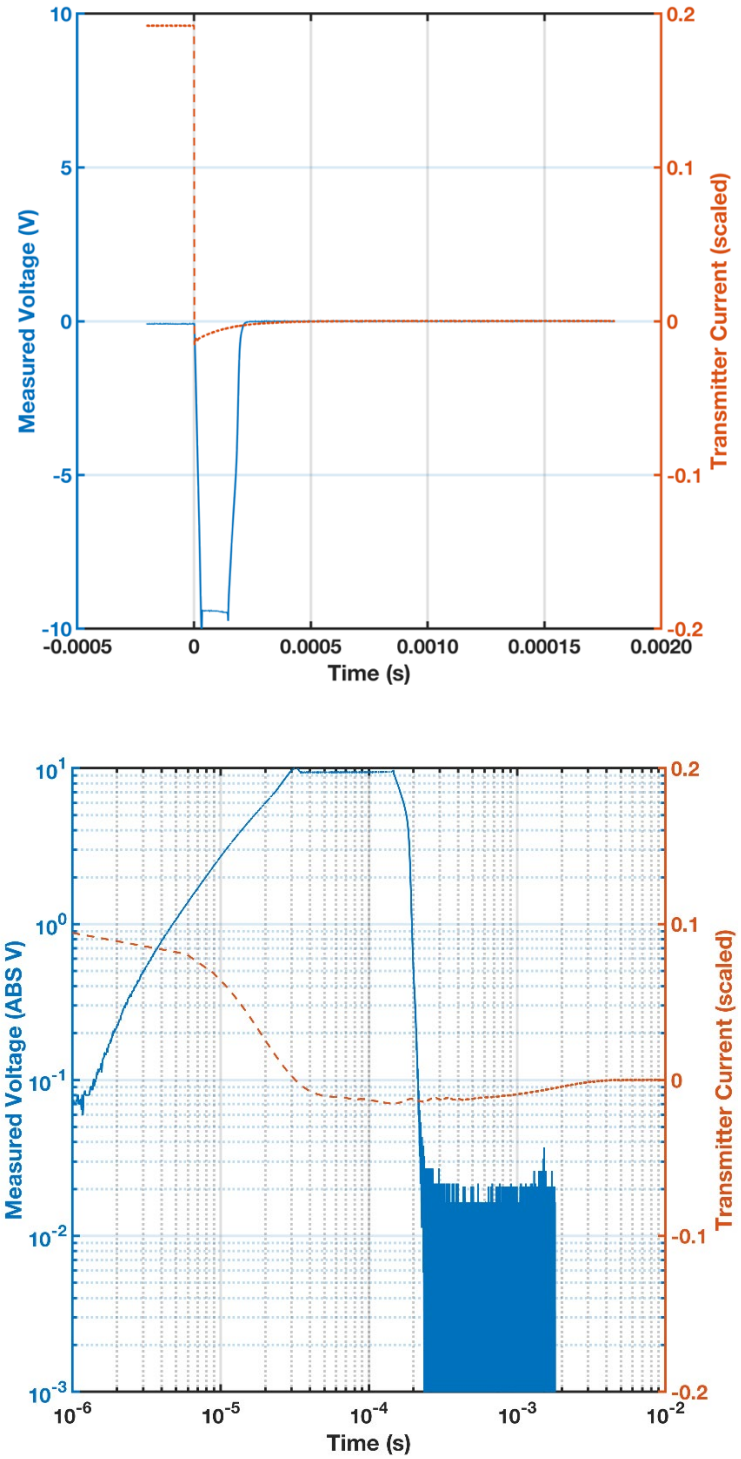

Figure A-31. Test 31. Linear and log-log presentation. Old motor, no propellers, on 25%, 32.5 cm offset, no target.

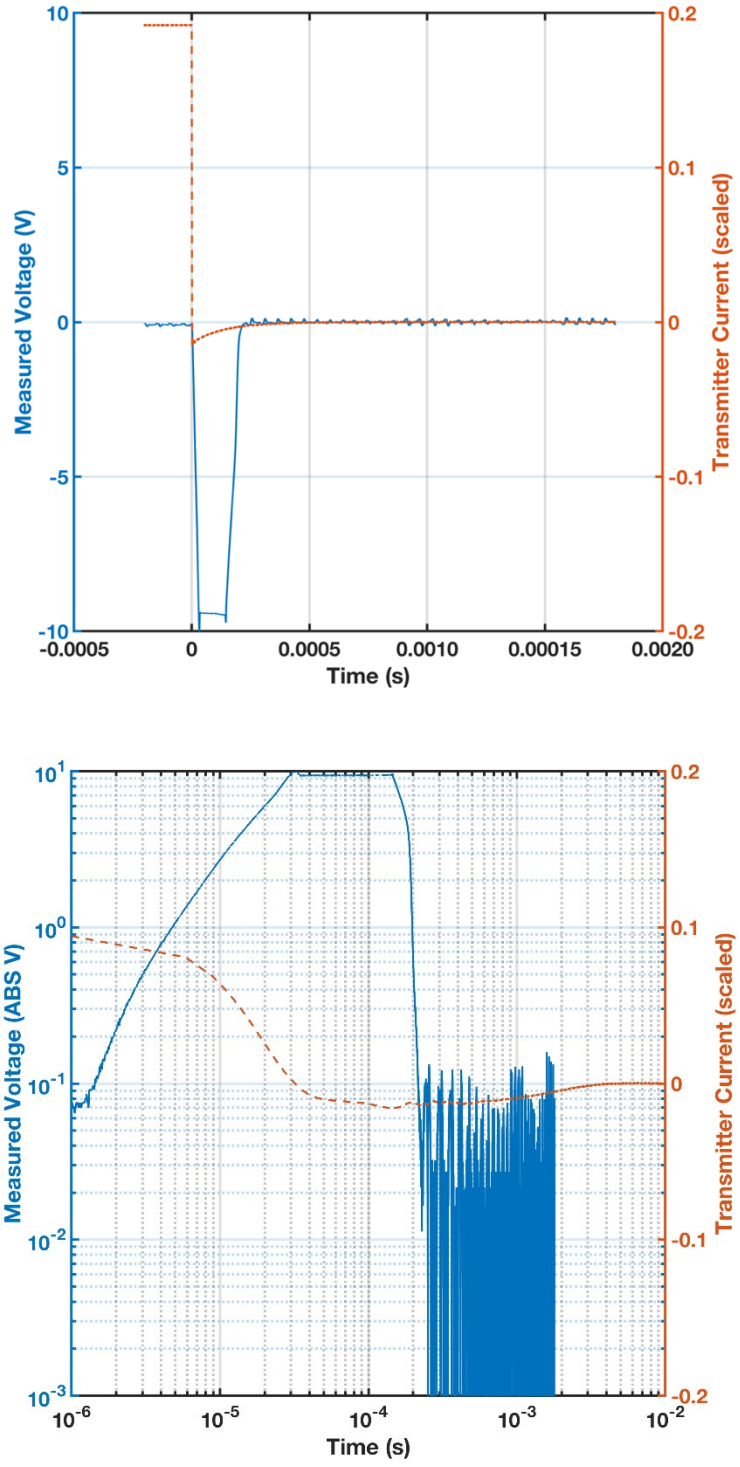

Figure A-32. Test 32. Linear and log-log presentation. Old motor, no propellers, on 50%, 32.5 cm offset, no target.

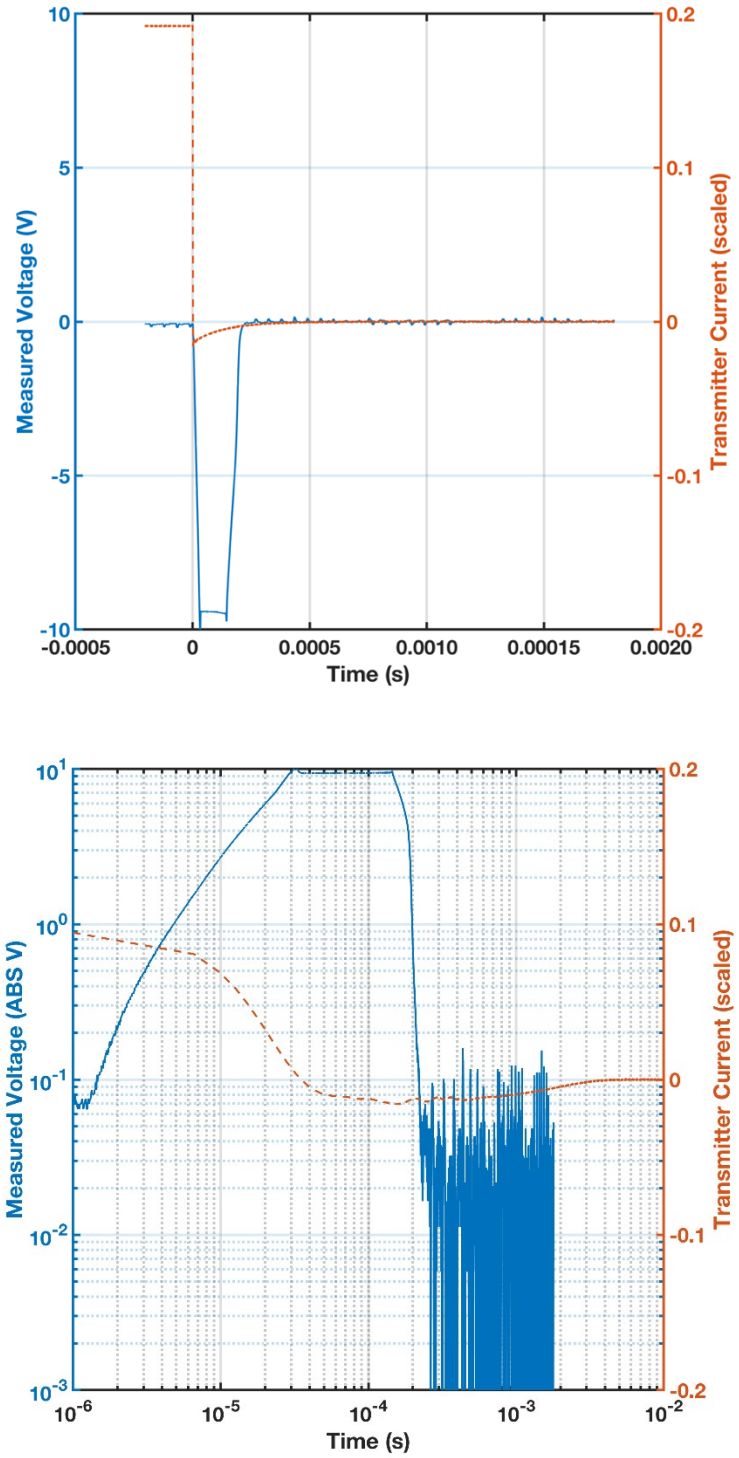

Figure A-33. Test 33. Linear and log-log presentation. Old motor, propellers attached, off, 32.5 cm offset, no target.

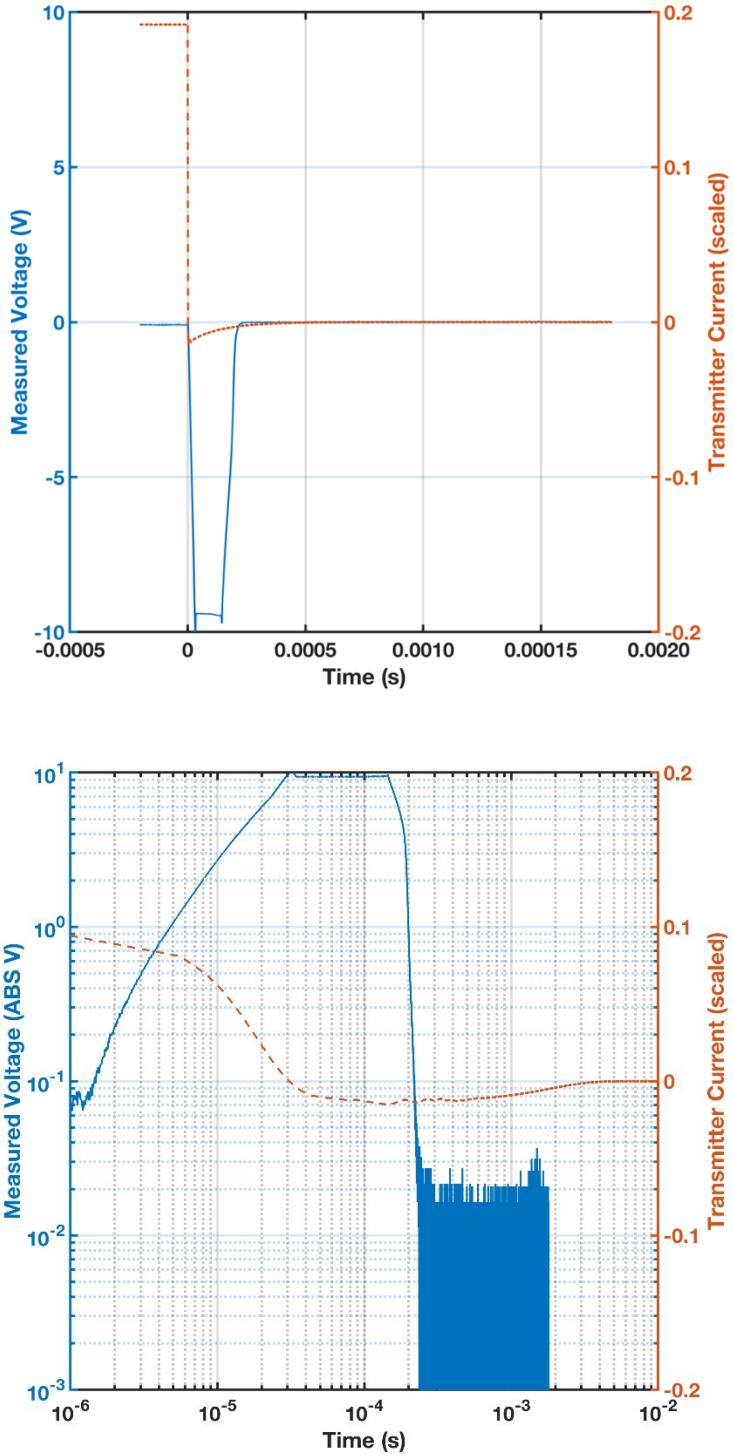

Figure A-34. Test 34 (data file irretrievably corrupted). Linear and log-log presentation. Old motor, propellers attached, on 25%, 32.5 cm offset, no target.

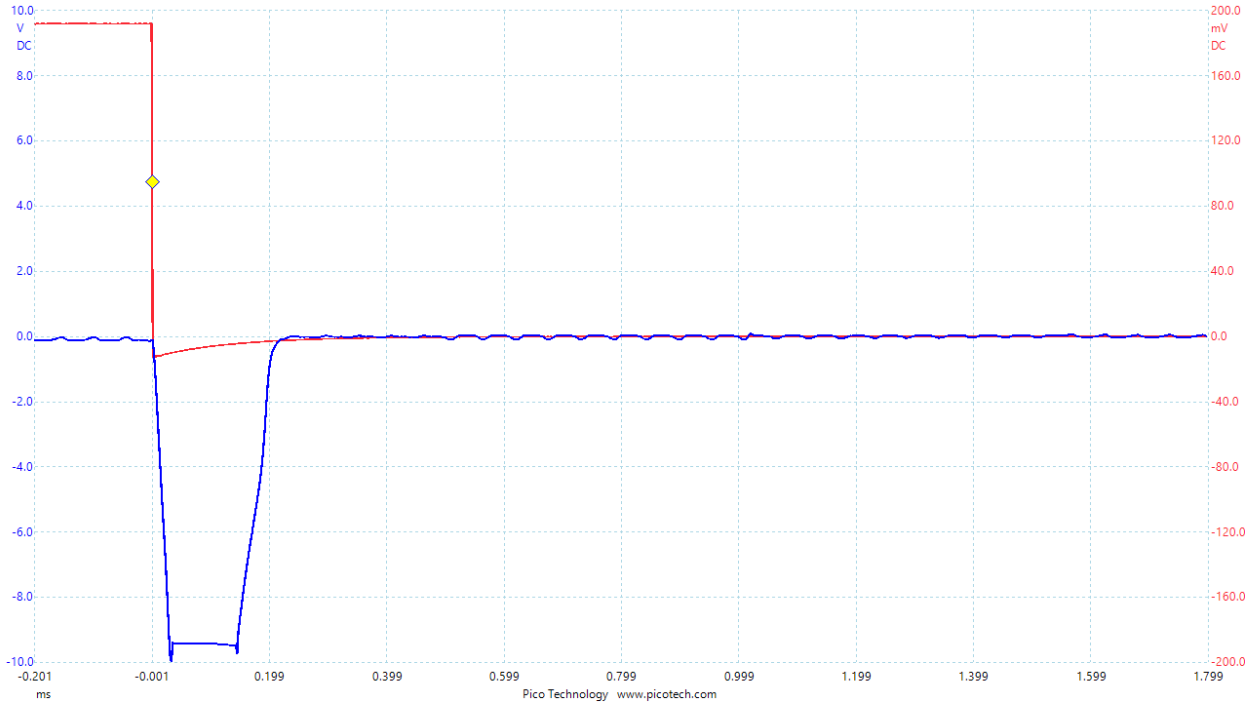

Figure A-35. Test 35. Linear and log-log presentation. Old motor, propellers attached, on 50%, 32.5 cm offset, no target.

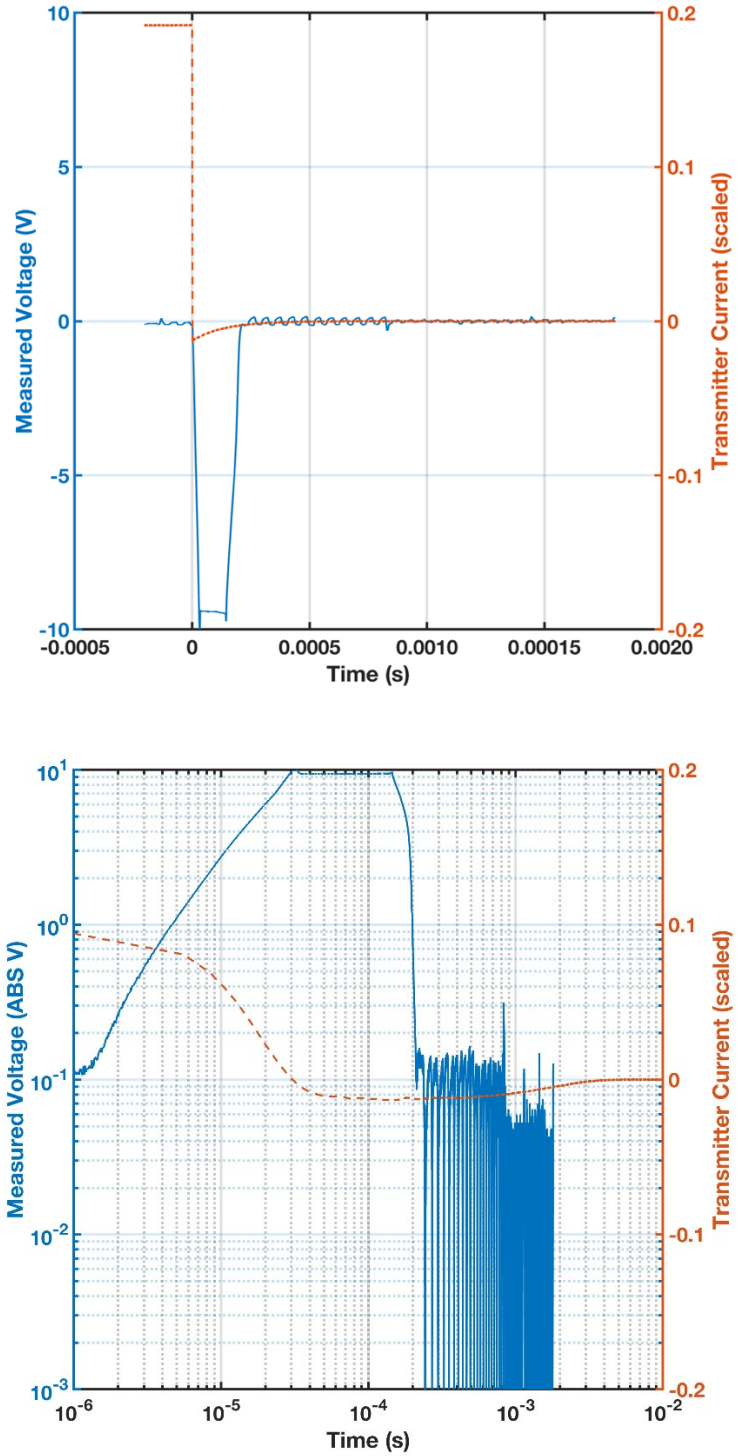

Figure A-36. Test 36. Linear and log-log presentation. New motor, propellers attached, off, 32.5 cm offset, no target.

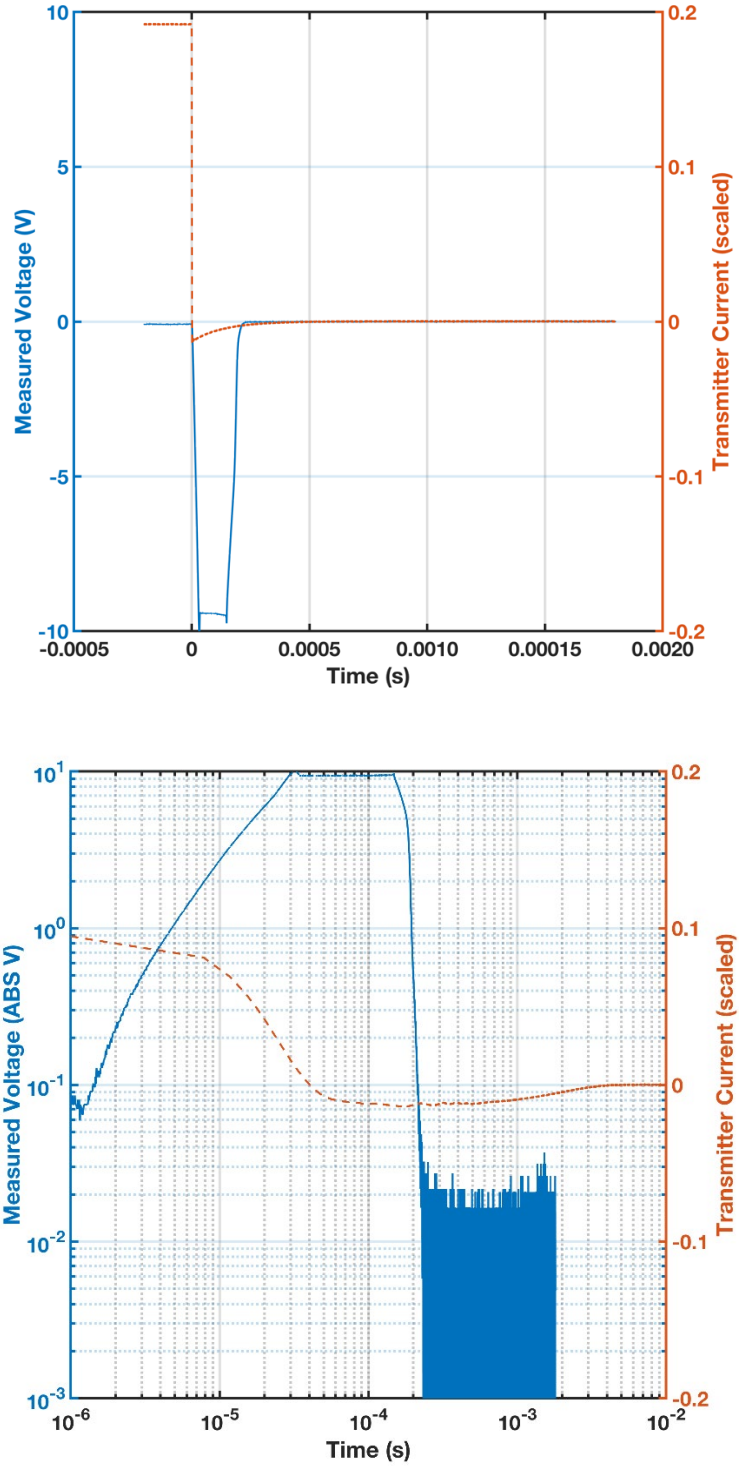

Figure A-37. Test 37. Linear and log-log presentation. New motor, propellers attached, on 25%, 32.5 cm offset, no target.

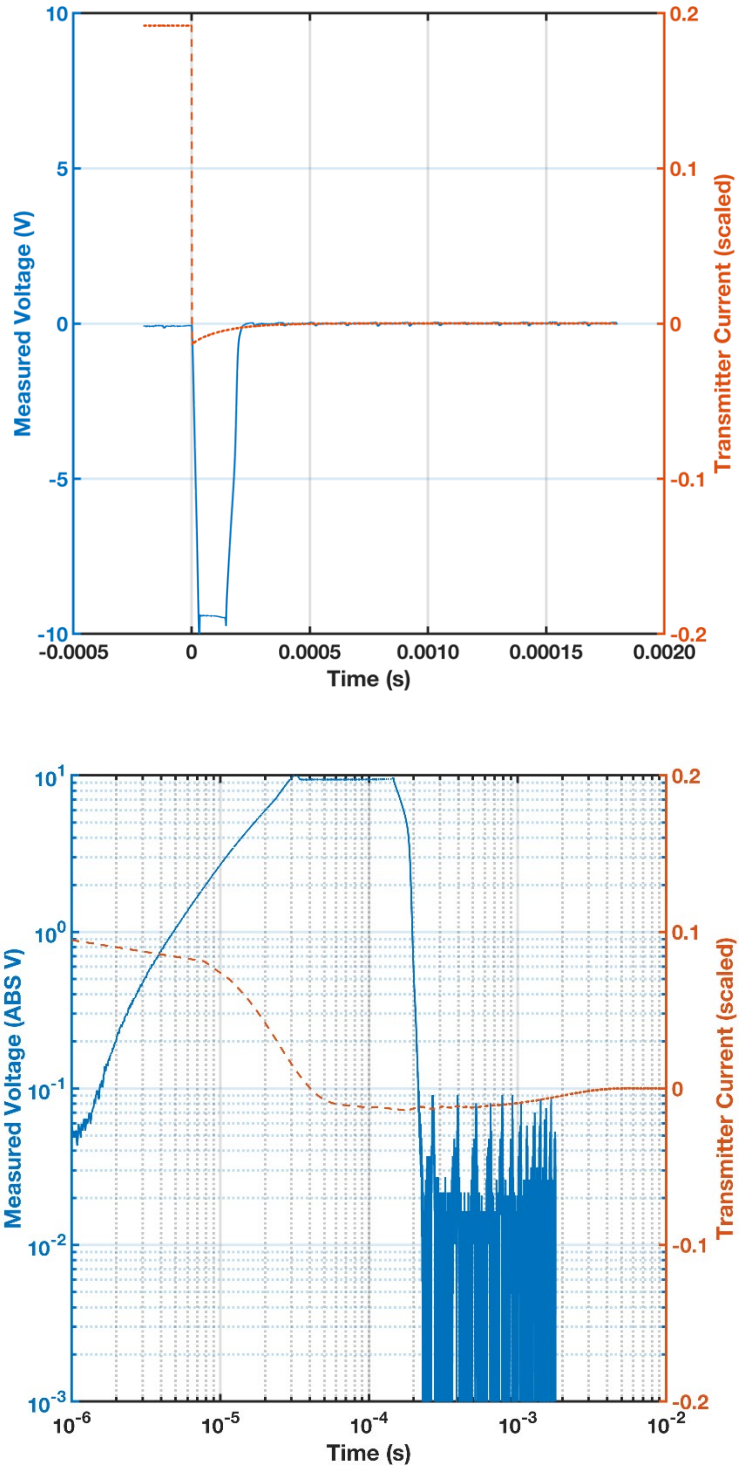

Figure A-38. Test 38. Linear and log-log presentation. New motor, propellers attached, on 50%, 32.5 cm offset, no target.

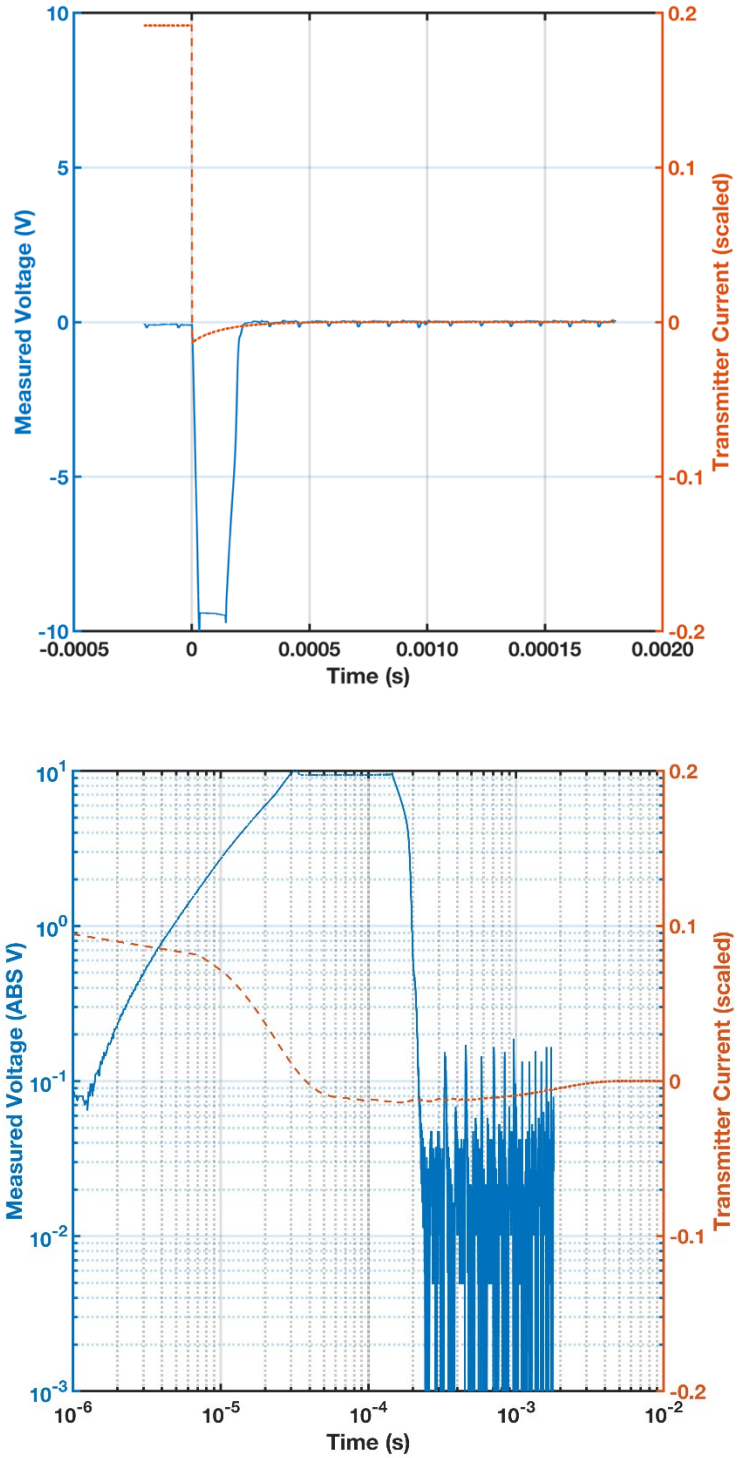

Figure A-39. Test 39. Linear and log-log presentation. New motor, propellers attached, off, 0 cm offset, no target.

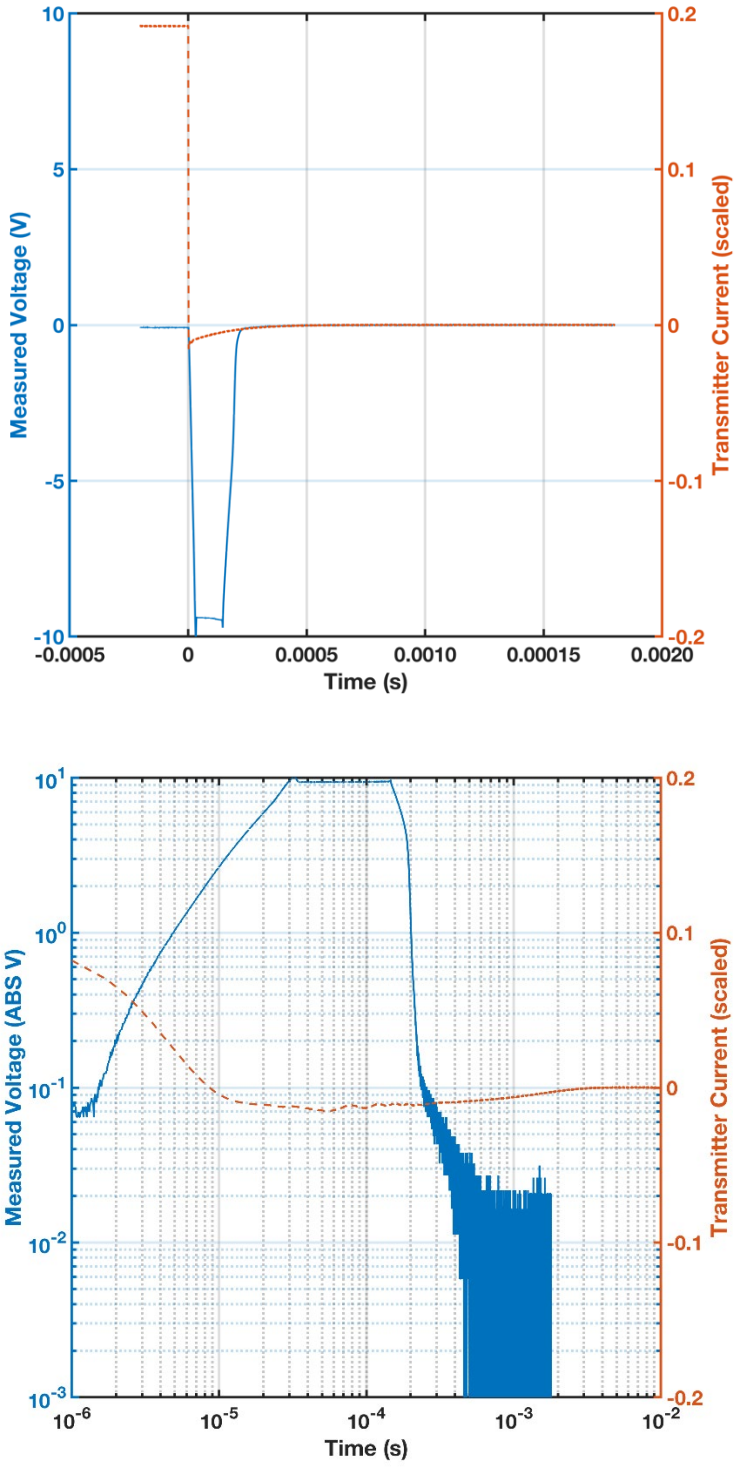

Figure A-40. Test 40. Linear and log-log presentation. New motor, propellers attached, on 25%, 0 cm offset, no target.

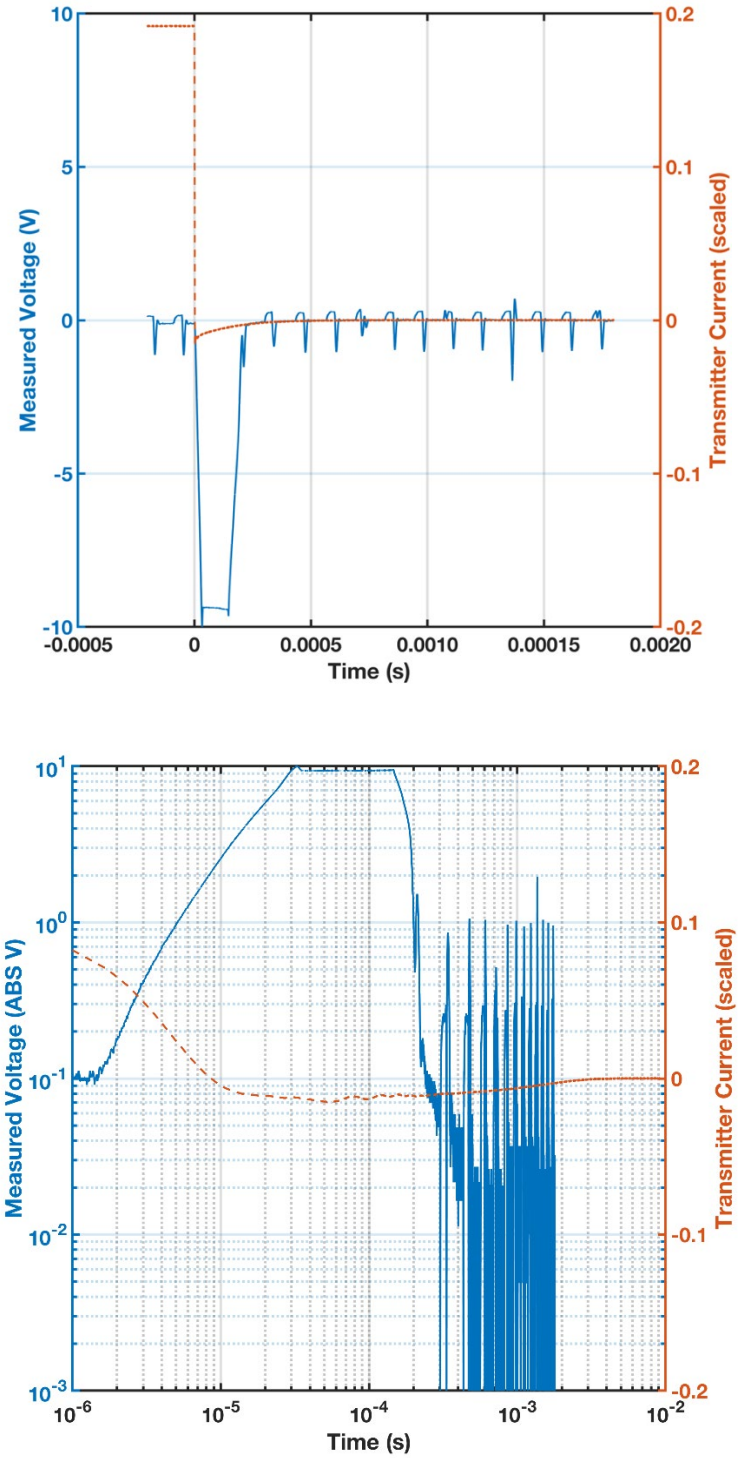

Figure A-41. Test 41. Linear and log-log presentation. New motor, propellers attached, on 50%, 0 cm offset, no target.

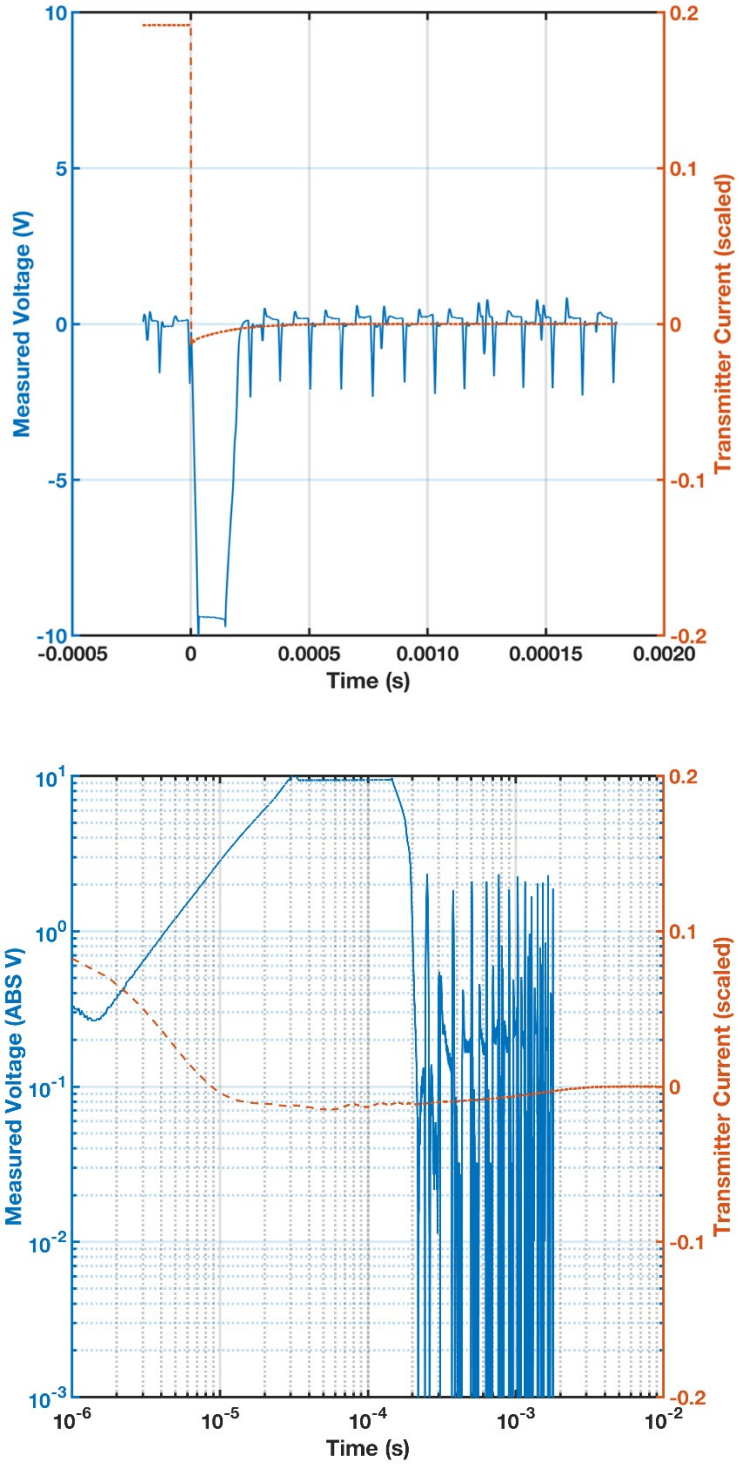

Figure A-42. Test 42. Linear and log-log presentation. New motor, propellers attached, off, 53 cm offset, no target.

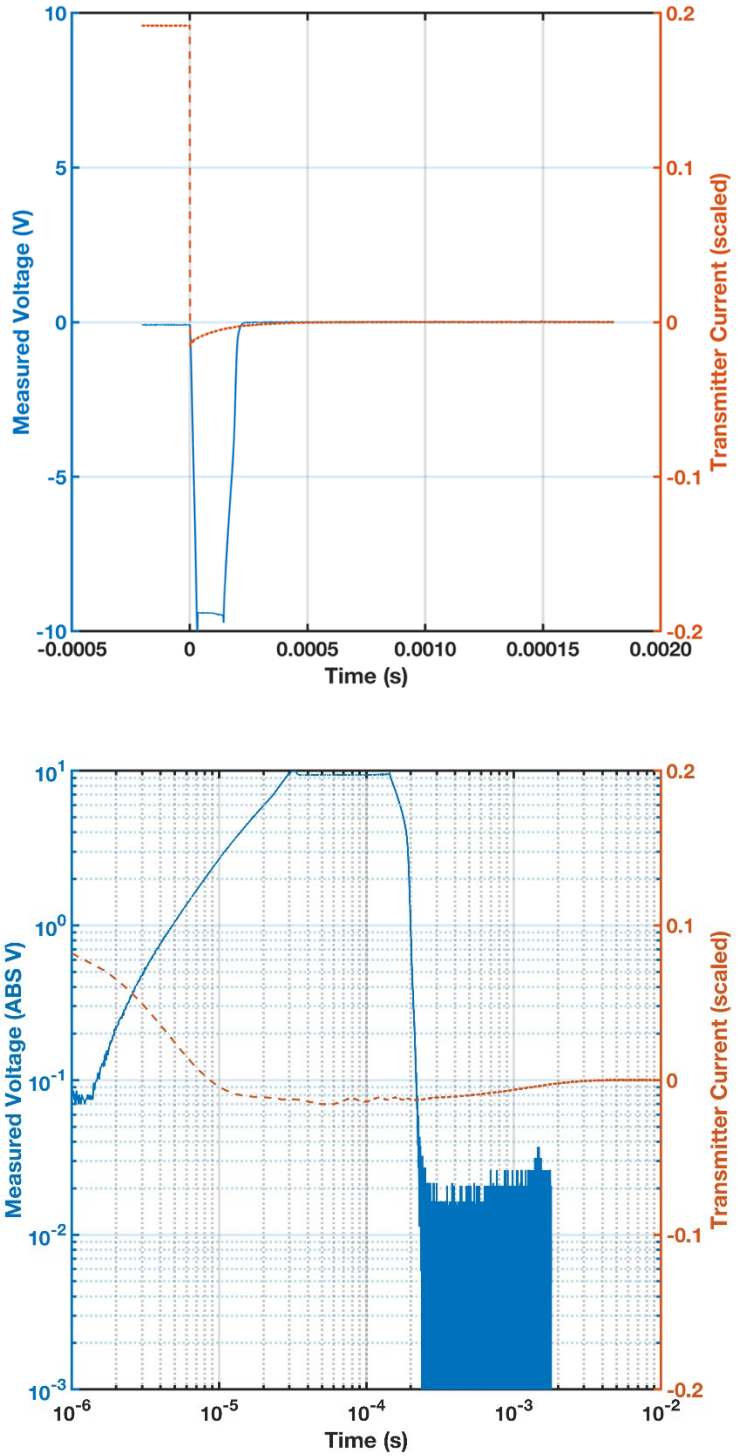

Figure A-43. Test 43. Linear and log-log presentation. New motor, propellers attached, on 25%, 53 cm offset, no target.

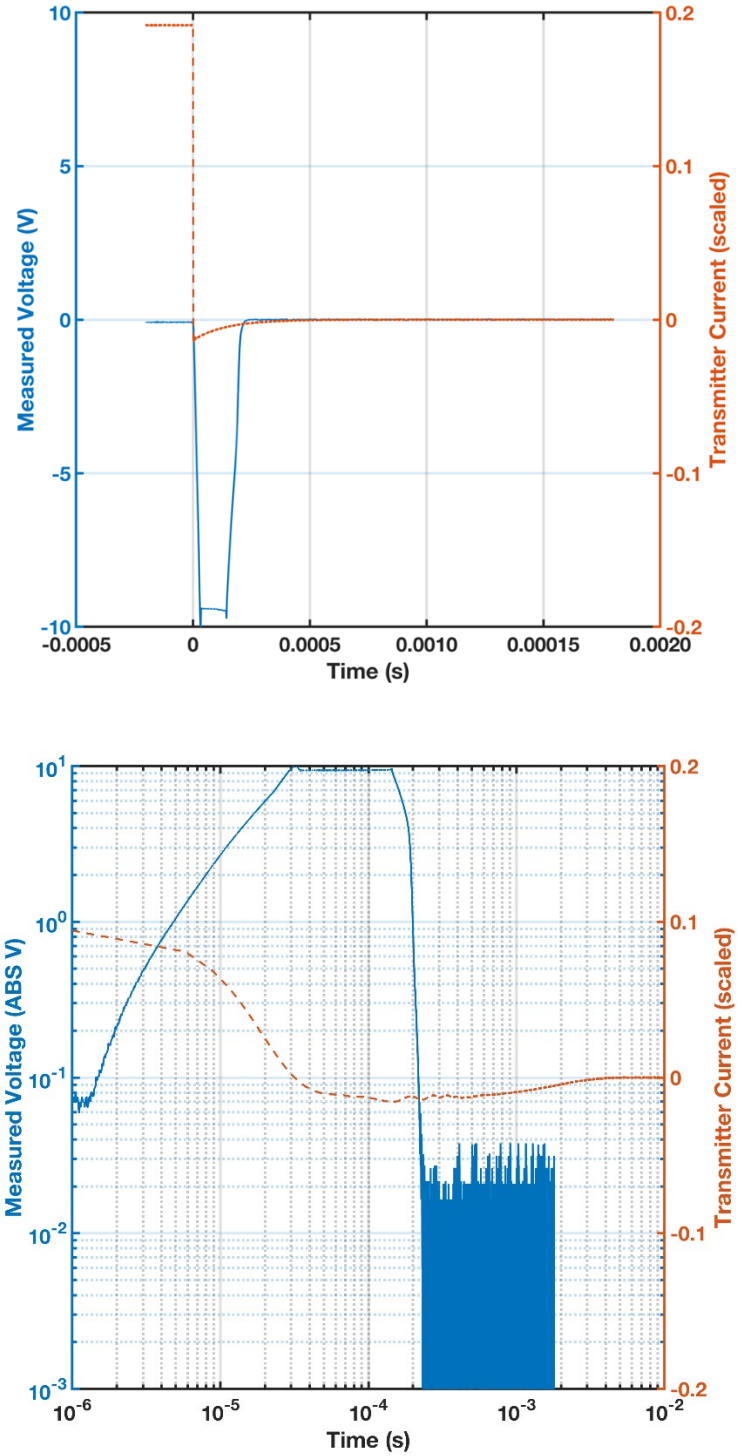

Figure A-44. Test 44. Linear and log-log presentation. New motor, propellers attached, on 50%, 53 cm offset, no target.

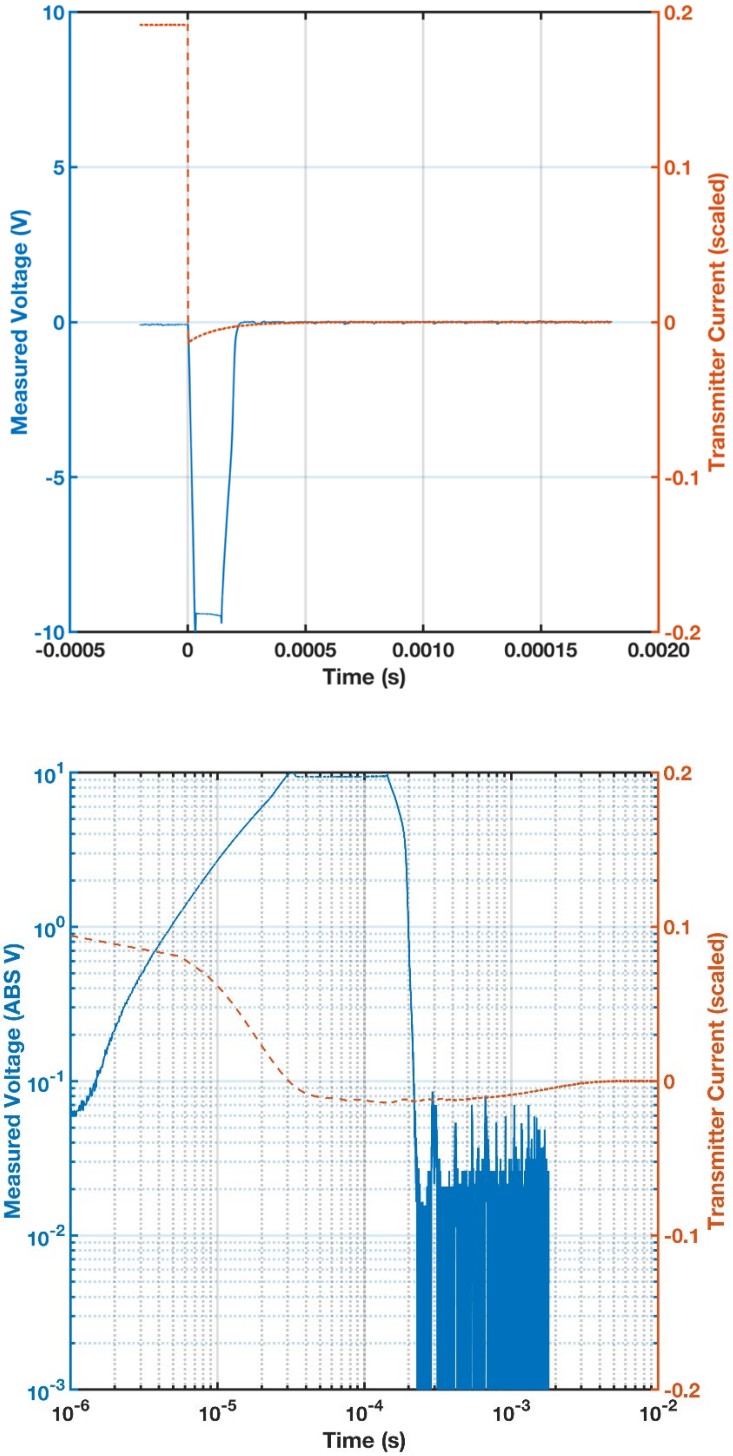

REPORT DOCUMENTATION PAGE

Form Approved
OMB No. 0704-0188

1. REPORT DATE *(DD-MM-YYYY)*
September 2019

2. REPORT TYPE
Technical Report/Final

3. DATES COVERED *(From - To)*

4. TITLE AND SUBTITLE

Unmanned Aerial Systems Electromagnetic Induction Sensor Development: Evaluation of Commercial-off-the-Shelf Unmanned Aerial System Motor Interference and Mitigation in Airborne Electromagnetic Induction Sensors

5a. CONTRACT NUMBER

5b. GRANT NUMBER

5c. PROGRAM ELEMENT NUMBER
PE 62784

6. AUTHOR(S)

Benjamin Barrowes, Dan R. Glaser, Brian G. Quinn, Mikheil Prishvin, and Fridon Shubitidze

5d. PROJECT NUMBER
T53

5e. TASK NUMBER

5f. WORK UNIT NUMBER

7. PERFORMING ORGANIZATION NAME(S) AND ADDRESS(ES)

U.S. Army Engineer Research and Development Center
Cold Regions Research and Engineering Laboratory
72 Lyme Road
Hanover, NH 03755-1290

Dartmouth College
Thayer School of Engineering
14 Engineering Drive
Hanover, NH 03755

8. PERFORMING ORGANIZATION REPORT NUMBER

ERDC/CRREL TR-19-20

9. SPONSORING / MONITORING AGENCY NAME(S) AND ADDRESS(ES)
United States Air Force Civil Engineer Center and U.S. Army Corps of Engineers
Tyndall Air Force Base, FL 32403

10. SPONSOR/MONITOR'S ACRONYM(S)
USACE

11. SPONSOR/MONITOR'S REPORT NUMBER(S)

12. DISTRIBUTION / AVAILABILITY STATEMENT
Approved for public release; distribution is unlimited.

13. SUPPLEMENTARY NOTES

Additional funding by FY17 Do3F Congressional Add for "Unmanned Aircraft Systems Sensor Integration"

14. ABSTRACT

The U.S. Army Cold Regions Research and Engineering Laboratory (CRREL) is supporting the U.S. Air Force Civil Engineer Center through research and development of an unmanned aerial system (UAS)–mounted electromagnetic induction (EMI) device capable of localizing embedded unexploded ordinance (UXO) for expedited runway and military range remediation. While EMI sensors exist for UXO detection, there are currently no UAS-based EMI systems that can provide this remote characterization of UXO with a near-real-time target classification. Developing and delivering this capability will provide a distinct improvement in soldiers' ability to quickly and efficiently recover from an attack.

Additionally, no expeditionary solutions presently exist for mapping of permafrost extent from medium-scale airborne platforms. This capability will allow lateral mapping of permafrost for impact assessments of construction activities, in a cost effective, standoff platform.

This study used the CRREL-Dartmouth-developed EMI sensor to measure the fields emitted by two different UAS motor configurations at varying standoff distances ranging from 0 to 53 cm. The minimal platform-to-sensor standoff distance was determined to be 60 cm for the planned frequency ranges. This specification will be used to design and construct the frame that carries the EMI transmitting and receiving sensor on the bottom of the UAS system.

15. SUBJECT TERMS
Electromagnetic Induction, Improvised Explosive Devices, Permafrost, Remote Sensing, Unexploded Ordinance, Unmanned Aerial Systems, Unmanned Aerial Vehicles

16. SECURITY CLASSIFICATION OF:			**17. LIMITATION OF ABSTRACT**	**18. NUMBER OF PAGES**	**19a. NAME OF RESPONSIBLE PERSON**
a. REPORT	**b. ABSTRACT**	**c. THIS PAGE**			**19b. TELEPHONE NUMBER** *(include area code)*
Unclassified	Unclassified	Unclassified	SAR	73	